

The Multiparameter Frontier: Metrological Hierarchy and Robustness in Dispersive Quantum Interferometry

Lucas Ferreira R. de Moura,¹ Daniel Y. Akamatsu,¹ G. D. de Moraes Neto ,^{2,*} and Norton G. de Almeida ,^{1,3}

¹*Instituto de Física, Universidade Federal de Goiás, 74.001-970, Goiânia - GO, Brazil*

²*Faculty of Civil Engineering and Mechanics, Kunming University of Science and Technology, Kunming, 650500, China*

³*Instituto de Física de São Carlos, Universidade de São Paulo,
Caixa Postal 369, 13560-970, São Carlos - SP, Brazil.*

Multiparameter quantum metrology—the simultaneous estimation of several physical quantities—represents a critical frontier for quantum sensing, promising enhanced sensor versatility but often limited by measurement incompatibility and environmental noise. We introduce a dispersive quantum thermometry protocol that utilizes a nonlinear Mach–Zehnder interferometer coupled to a thermal ancilla to jointly estimate the inverse temperature β and a dispersive interaction strength x . Our analysis yields closed analytical expressions for the entire quantum Fisher information matrix, revealing that the metrological performance is governed solely by a single physical quantity: the *thermal visibility* $\mathcal{V}(\beta)$ and its derivative. A key feature of the scheme is that the output optical state remains diagonal in the photon-number basis; consequently, simple photon counting is globally optimal and saturates the multiparameter quantum Cramér–Rao bound without any adaptive feedback. Moving beyond the ideal unitary limit, we critically evaluate the protocol’s robustness under the concurrent action of amplitude and phase damping. By analyzing the *Fisher Information Susceptibility*, we establish a clear metrological hierarchy for realistic open systems: while NOON states provide maximal peak sensitivity in theory, they exhibit an exponential fragility to loss that renders their advantage illusory in practice. In contrast, we identify Squeezed Vacuum states as a robust alternative for steady-state sensing and standard Cat states as a compelling candidate for transient thermometry, as they avoid the catastrophic decoherence of NOON states by retaining significant coherence even after photon loss. We validate these predictions by implementing the protocol as a digital quantum circuit on the IBM Quantum `ibm_torino` processor. The experimental results not only confirm the predicted Fisher information landscape but also expose systematic noise-induced biases, demonstrating that current NISQ-era hardware can already serve as effective testbeds for benchmarking the fundamental trade-offs in multiparameter quantum sensing.

I. INTRODUCTION

Quantum metrology harnesses quantum resources—such as coherence, entanglement, and non-classical light—to achieve a fundamental enhancement in the precision of estimating physical parameters, surpassing classical limits [1–8]. In this framework, the ultimate precision bounds are governed by the classical Fisher information (FI) and its quantum generalization, the quantum Fisher information (QFI), which appear in the Cramér–Rao inequalities for unbiased estimators [4, 9–15]. When multiple parameters are estimated simultaneously, these bounds are dictated by the full Fisher-information matrix. In this multiparameter setting, non-trivial trade-offs can arise from statistical correlations and from the potential incompatibility of the optimal measurements for different parameters [15–22].

Multiparameter quantum metrology is particularly relevant in scenarios where a single experimental platform must be calibrated or characterized with respect to several unknown quantities at once. Key examples include quantum imaging and sensing [7, 8, 23–30], the simultaneous estimation of phase and loss in interferometry [1, 2, 31–33], and quantum thermometry where tem-

perature must be inferred alongside unknown Hamiltonian parameters [20, 34–51]. Experimentally, nanoscale and solid-state quantum thermometry have been realized using luminescent nanothermometers, color centers in diamond, and circuit- or optomechanical platforms [52–58]. In such contexts, it is often advantageous to design a single protocol that yields information about all relevant parameters from one measurement record, rather than performing separate, independent estimations [59–61].

Optical interferometers, most notably the Mach–Zehnder interferometer (MZI), serve as a natural and flexible testbed for this task [31–33, 62–67]. They allow parameters to be encoded into relative phases or via dispersive light–matter interactions and can operate with a wide variety of quantum input states. Concurrently, the field of digital quantum simulation enables the implementation of these schemes as quantum circuits, where beam splitters and interactions are mapped onto sequences of unitary gates acting on qubits [68–79].

In this work, we investigate a model in which an optical field interacts dispersively with a thermalized two-level system placed in one arm of an MZI [80]. The Hamiltonian governing the interaction is

$$\hat{H} = \hbar\chi \hat{a}^\dagger \hat{a} \hat{\sigma}_+ \hat{\sigma}_-, \quad (1)$$

leading to the evolution operator

$$\hat{U} = e^{-ix\hat{a}^\dagger \hat{a} \hat{\sigma}_+ \hat{\sigma}_-}, \quad x = \chi t, \quad (2)$$

* gdmneto@gmail.com

where t is the interaction time, χ the dispersive coupling strength, x the resulting dimensionless dispersive phase, \hat{a} the optical annihilation operator, and $\hat{\sigma}_+ \hat{\sigma}_- = |e\rangle\langle e|$ the projector onto the atomic excited state. Such qubit- or impurity-based probes have been extensively studied in quantum thermometry and dephasing-based sensing [81–86].

This study extends our recent single-parameter analysis of dispersive quantum thermometry [79] to the multi-parameter regime. In that prior study, we refuted claims of Heisenberg-limited scaling for temperature estimation in such a setup, demonstrating that while the Hamiltonian parameter x can benefit from quantum enhancement, the precision for temperature remains constrained by the standard quantum limit. A distinctive feature of our current multiparameter model is that the output optical state remains diagonal in the photon-number basis. Consequently, the QFI matrix coincides exactly with the classical FI matrix, meaning that simple photon-number counting constitutes an optimal measurement, saturating the multiparameter quantum Cramér–Rao bound [13–15, 87]. We derive closed analytical expressions for all elements of the FI matrix and introduce scalar figures of merit to quantify the overall quality of joint estimation.

However, moving beyond the ideal unitary limit, we critically address the *Multiparameter Frontier* of practical sensing: the protocol’s robustness under the concurrent action of Amplitude Damping (AD) and Phase Damping (PD)—two dominant noise channels in realistic quantum hardware. Using the framework of *Fisher Information Susceptibility* (χ_F) [88], we rigorously formalize the impact of decoherence. We demonstrate that while NOON states exhibit a quadratic sensitivity to phase noise ($\chi_F^{\text{PD}} \propto N^2$), they suffer from a cubic susceptibility to amplitude damping ($\chi_F^{\text{AD}} \propto N^3$). This identifies photon loss as the dominant mechanism that confines their quantum advantage to a strictly noise-free manifold. In contrast, we identify Squeezed Vacuum states as a robust alternative for steady-state sensing, and standard Cat states as a compelling intermediate candidate, avoiding catastrophic decoherence by retaining significant coherence even after photon loss.

Complementing the analytical treatment, we construct a quantum circuit that faithfully reproduces the action of the nonlinear MZI. Simulations of this circuit validate our theoretical predictions across a broad parameter range. Finally, we execute the protocol on the IBM Quantum Experience platform (`ibm_torino`). The experimental results not only reproduce the qualitative features of the Fisher information landscape but also reveal systematic biases that serve as a direct signature of the amplitude damping channel. This combined approach—linking fundamental analytical bounds to hardware-specific noise signatures—provides a holistic perspective on the capabilities and limitations of quantum multiparameter sensors in the NISQ era [89, 90].

The paper is organized as follows. Section II reviews the classical and quantum Fisher information formalism.

Section III presents the interferometric model and derives the optimal measurement strategy. Section IV details the digital quantum circuit implementation. Section V D presents the experimental validation on IBM Quantum hardware. Section VI provides a deep-dive robustness analysis, establishing the metrological hierarchy and explaining the observed experimental deviations. Finally, Sec. VII summarizes our findings and outlines future directions, including applications to time crystals and distributed sensing networks.

II. QUANTUM MULTIPARAMETER ESTIMATION

In this section we briefly review the basic tools of classical and quantum multiparameter estimation that will be used throughout the paper. We follow standard treatments of quantum metrology and quantum estimation theory, adapting the notation to our specific two-parameter problem.

A. Classical Fisher information

Let $\boldsymbol{\theta} = (\theta_1, \theta_2, \dots, \theta_p)^\top$ denote a vector of p real parameters to be estimated from the outcomes y of a measurement described by a conditional probability distribution $p(y|\boldsymbol{\theta})$. An estimator $\hat{\boldsymbol{\theta}}(y)$ is a function of the observed data, and its performance is characterized by the covariance matrix

$$\text{Cov}(\hat{\boldsymbol{\theta}})_{ab} = \langle (\hat{\theta}_a - \theta_a)(\hat{\theta}_b - \theta_b) \rangle, \quad (3)$$

where the average is taken with respect to $p(y|\boldsymbol{\theta})$. For unbiased estimators, $\langle \hat{\theta}_a \rangle = \theta_a$, the covariance matrix is bounded from below by the inverse of the classical Fisher-information matrix (FIM) $F(\boldsymbol{\theta})$, whose elements are defined as

$$F_{ab}(\boldsymbol{\theta}) = \sum_y \frac{1}{p(y|\boldsymbol{\theta})} \frac{\partial p(y|\boldsymbol{\theta})}{\partial \theta_a} \frac{\partial p(y|\boldsymbol{\theta})}{\partial \theta_b}, \quad (4)$$

for discrete outcomes y . In matrix form, the multiparameter Cramér–Rao bound (CRB) reads

$$\text{Cov}(\hat{\boldsymbol{\theta}}) \succeq \frac{1}{\mu} F(\boldsymbol{\theta})^{-1}, \quad (5)$$

where μ is the number of independent repetitions of the experiment and $A \succeq B$ means that $A - B$ is a positive semidefinite matrix. In particular, for any real weight vector \mathbf{c} one has

$$\mathbf{c}^\top \text{Cov}(\hat{\boldsymbol{\theta}}) \mathbf{c} \geq \frac{1}{\mu} \mathbf{c}^\top F(\boldsymbol{\theta})^{-1} \mathbf{c}, \quad (6)$$

showing that the FIM encapsulates all attainable precisions for unbiased estimators built from the chosen measurement statistics.

B. Quantum Fisher-information matrix and quantum Cramér–Rao bound

In the quantum setting, the parameters $\boldsymbol{\theta}$ are encoded in a family of density operators $\hat{\rho}(\boldsymbol{\theta})$ acting on a Hilbert space \mathcal{H} . A general measurement is described by a positive operator-valued measure (POVM) $\{\hat{\Pi}_y\}$, with $\hat{\Pi}_y \geq 0$ and $\sum_y \hat{\Pi}_y = \mathbb{I}$, leading to the Born probabilities

$$p(y|\boldsymbol{\theta}) = \text{Tr}[\hat{\rho}(\boldsymbol{\theta})\hat{\Pi}_y]. \quad (7)$$

For each POVM, the associated classical Fisher-information matrix $F(\boldsymbol{\theta})$ is given by Eq. (4). Optimizing over all POVMs yields the quantum Fisher-information matrix (QFIM) $Q(\boldsymbol{\theta})$, whose elements can be expressed in terms of the symmetric logarithmic derivatives (SLDs) \hat{L}_a defined implicitly by

$$\frac{\partial \hat{\rho}(\boldsymbol{\theta})}{\partial \theta_a} = \frac{1}{2}(\hat{\rho}(\boldsymbol{\theta})\hat{L}_a + \hat{L}_a\hat{\rho}(\boldsymbol{\theta})). \quad (8)$$

The QFIM elements are then

$$Q_{ab}(\boldsymbol{\theta}) = \frac{1}{2} \text{Tr}[\hat{\rho}(\boldsymbol{\theta})(\hat{L}_a\hat{L}_b + \hat{L}_b\hat{L}_a)]. \quad (9)$$

The quantum Cramér–Rao bound (QCRB) states that the covariance matrix of any unbiased estimator satisfies

$$\text{Cov}(\hat{\boldsymbol{\theta}}) \succeq \frac{1}{\mu} Q(\boldsymbol{\theta})^{-1}, \quad (10)$$

for any physically allowed measurement strategy. Since $F(\boldsymbol{\theta}) \leq Q(\boldsymbol{\theta})$ in the matrix sense, the QFIM sets the ultimate precision limits allowed by quantum mechanics.

In the single-parameter case ($p = 1$), the QCRB is always saturable in the asymptotic limit $\mu \rightarrow \infty$. For multiple parameters, however, the situation is more subtle: in general, there may not exist a single POVM that simultaneously achieves the quantum-limited precision for all components of $\boldsymbol{\theta}$. A necessary condition for the simultaneous saturation of the QCRB for all parameters is the weak commutativity condition $\text{Tr}(\rho[\hat{L}_a, \hat{L}_b]) = 0$. For the existence of a single-copy measurement achieving $F(\boldsymbol{\theta}) = Q(\boldsymbol{\theta})$, a sufficient condition is the strong commutativity $[\hat{L}_a, \hat{L}_b] = 0$. However, under the weak commutativity condition, the QCRB can be asymptotically saturated for all parameters simultaneously using collective measurements on infinitely many copies.

C. Figures of merit for joint estimation

In a multiparameter scenario, there is no unique *best* figure of merit, since the covariance matrix encodes trade-offs between the variances and covariances of different parameters. A common approach is to consider a weighted sum of variances

$$\Delta_{\mathbf{w}}^2(\hat{\boldsymbol{\theta}}) = \sum_{a,b} w_{ab} \text{Cov}(\hat{\boldsymbol{\theta}})_{ab}, \quad (11)$$

with a positive semidefinite cost matrix $W = (w_{ab})$. The CRB then implies

$$\Delta_{\mathbf{w}}^2(\hat{\boldsymbol{\theta}}) \geq \frac{1}{\mu} \text{Tr}[W F(\boldsymbol{\theta})^{-1}] \geq \frac{1}{\mu} \text{Tr}[W Q(\boldsymbol{\theta})^{-1}]. \quad (12)$$

In the absence of a preferred cost matrix, one may adopt scalar indicators that are invariant under permutations of the parameters. Two natural choices are:

- the total variance $\text{Tr}[\text{Cov}(\hat{\boldsymbol{\theta}})]$, bounded below by $(1/\mu) \text{Tr}[F(\boldsymbol{\theta})^{-1}]$;
- the determinant of the covariance matrix, whose inverse is bounded from above by $\mu^p \det F(\boldsymbol{\theta})$ and is related to the volume of the uncertainty ellipsoid in parameter space.

In what follows, we will focus on the $p = 2$ case, $\boldsymbol{\theta} = (\beta, x)^\top$, and introduce an effective Fisher information

$$F_{\text{eff}}(\beta, x) = \frac{\det F(\beta, x)}{\text{Tr } F(\beta, x)}, \quad (13)$$

which provides a single scalar quantifier of how well conditioned the simultaneous estimation of both parameters is. In this two-parameter setting we adopt the simplest choice $W = \mathbb{I}$, so that β and x are weighted equally in the multiparameter figure of merit. Large values of F_{eff} correspond to small joint uncertainties and to a FIM that is neither nearly singular nor strongly dominated by a single parameter. When the optimal measurement is known and satisfies $F(\beta, x) = Q(\beta, x)$, the same definition can be used with the QFIM. In Sec. III we show that this is precisely the case for the interferometric model considered in this work.

III. PHYSICAL MODEL AND ANALYTICAL FISHER INFORMATION

A. Mach–Zehnder interferometer with a thermal atom

We consider a Mach–Zehnder interferometer (MZI) in which a light field interacts dispersively with a two-level atom located in one of the interferometer arms, as schematically illustrated in Fig. 1. The atomic transition $|g\rangle \leftrightarrow |e\rangle$ has energy splitting $\hbar\omega_0$, and the dispersive light–matter coupling is described by the effective Hamiltonian and the corresponding unitary operator is given by Eq. (2), which imprints on the optical field a phase shift proportional to the photon number if and only if the atom is in the excited state.

The atom is initially prepared in a thermal (Gibbs) state characterized by the inverse temperature $\beta = 1/(k_B T)$,

$$\hat{\rho}_A(\beta) = \frac{1}{Z_\beta} \begin{pmatrix} e^{-\beta\hbar\omega_0} & 0 \\ 0 & 1 \end{pmatrix}, \quad Z_\beta = 1 + e^{-\beta\hbar\omega_0}. \quad (14)$$

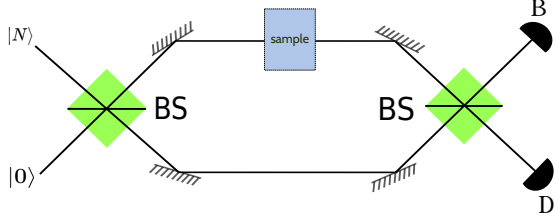


FIG. 1. Schematic of the Mach-Zehnder interferometer (MZI) built with nonlinear beam splitters (BS) used in this work. A NOON state of N photons enters the interferometer and, in one of the arms, the light field interacts dispersively with a two-level atom (sample) prepared in a thermal state at inverse temperature β . B and D denote detectors at the output ports.

The optical input of the MZI is taken to be a NOON state of N photons,

$$|\psi_{\text{in}}\rangle = \frac{1}{\sqrt{2}}(|N,0\rangle + |0,N\rangle), \quad (15)$$

which provides the maximal phase sensitivity allowed by the optical resources. Following Ref. [79], we prepare the NOON state and consider the action of a nonlinear beam splitter on this state, which leads to the following transformations:

$$\begin{aligned} |N\rangle_a \otimes |0\rangle_b &\equiv |N,0\rangle \longrightarrow \frac{1}{\sqrt{2}}(|N,0\rangle + |0,N\rangle), \\ |0\rangle_a \otimes |N\rangle_b &\equiv |0,N\rangle \longrightarrow \frac{1}{\sqrt{2}}(|0,N\rangle - |N,0\rangle). \end{aligned} \quad (16)$$

B. Output probabilities and thermal visibility

After the first (nonlinear) beam splitter, the dispersive interaction acts only on the upper arm of the interferometer. In our implementation, the light-matter coupling is governed by $\hat{H} = \hbar\chi \hat{a}^\dagger \hat{a} \sigma_+ \sigma_- = \hbar\chi \hat{a}^\dagger \hat{a} |e\rangle \langle e|$, so that a phase is imprinted *only* when the atom is excited. After recombination at the second (also nonlinear) beam splitter, we perform photon-number measurements at one of the output ports, projecting the light onto $|0\rangle$ or $|N\rangle$.

Tracing over the atomic degree of freedom yields the classical probabilities

$$\begin{aligned} P_0(\beta, x) &= \frac{1 + \mathcal{V}(\beta) \cos(2Nx)}{1 + \mathcal{V}(\beta)}, \\ P_N(\beta, x) &= 1 - P_0(\beta, x) = \frac{2\mathcal{V}(\beta)}{1 + \mathcal{V}(\beta)} \sin^2(Nx), \end{aligned} \quad (17)$$

where we have defined the *fringe visibility*

$$\mathcal{V}(\beta) \equiv \mathcal{V}_{\text{std}} = \frac{P_{\text{max}} - P_{\text{min}}}{P_{\text{max}} + P_{\text{min}}} = \frac{e^{-\beta\hbar\omega_0}}{2 + e^{-\beta\hbar\omega_0}}, \quad (18)$$

with $P_{\text{max}} = 1$ (at $Nx = k\pi$) and $P_{\text{min}} = \frac{1-\mathcal{V}(\beta)}{1+\mathcal{V}(\beta)}$ (at $Nx = (k + \frac{1}{2})\pi$), for any integer k . Note that $\mathcal{V}(\beta)$

modulates the fringe contrast and is set by the thermal mixing between a phase-imprinting branch ($|e\rangle$) and a phase-free branch ($|g\rangle$). This visibility is a monotonic function of β : it approaches 0 in the cold (non-inverted) limit $\beta \rightarrow +\infty$ (where $p_e \rightarrow 0$ and $P_0 \rightarrow 1$), takes the intermediate value $\mathcal{V}(0) = 1/3$ at infinite temperature, and approaches 1 in the cold inverted limit $\beta \rightarrow -\infty$ (where $p_e \rightarrow 1$ and $P_0 \rightarrow \frac{1}{2}[1 + \cos(2Nx)] = \cos^2(Nx)$). Therefore, the fringe contrast encodes the temperature, including the sign of β (e.g., $\mathcal{V} > 1/3$ corresponds to $\beta < 0$ and $\mathcal{V} < 1/3$ to $\beta > 0$).

C. Analytical Fisher-information matrix

Because the measurement outcomes $\{0, N\}$ correspond to orthogonal projectors, the Fisher information associated with photon-number detection is purely classical. From Eqs. (17) and (18), the gradient of P_0 with respect to (β, x) reads

$$\begin{aligned} \partial_\beta P_0 &= \frac{2\hbar\omega_0 \mathcal{V}(\beta) [1 - \mathcal{V}(\beta)]}{[1 + \mathcal{V}(\beta)]^2} \sin^2(Nx), \\ \partial_x P_0 &= -\frac{2N \mathcal{V}(\beta)}{1 + \mathcal{V}(\beta)} \sin(2Nx). \end{aligned} \quad (19)$$

where we used $\mathcal{V}'(\beta) = -\hbar\omega_0 \mathcal{V}(\beta) [1 - \mathcal{V}(\beta)]$. Since the probabilities satisfy $P_N = 1 - P_0$, the Fisher-information matrix elements

$$F_{ab}(\beta, x) = \sum_{y \in \{0, N\}} \frac{1}{P_y} \frac{\partial P_y}{\partial \theta_a} \frac{\partial P_y}{\partial \theta_b}, \quad \boldsymbol{\theta} = (\beta, x)^\top, \quad (20)$$

can be written in closed form as

$$F_{\beta\beta} = \frac{(\partial_\beta P_0)^2}{P_0(1 - P_0)} = \frac{2(\hbar\omega_0)^2 \mathcal{V}(\beta) [1 - \mathcal{V}(\beta)]^2 \sin^2(Nx)}{[1 + \mathcal{V}(\beta)]^2 [1 + \mathcal{V}(\beta) \cos(2Nx)]}, \quad (21)$$

$$F_{xx} = \frac{(\partial_x P_0)^2}{P_0(1 - P_0)} = \frac{8N^2 \mathcal{V}(\beta) \cos^2(Nx)}{1 + \mathcal{V}(\beta) \cos(2Nx)}, \quad (22)$$

$$F_{\beta x} = \frac{\partial_\beta P_0 \partial_x P_0}{P_0(1 - P_0)} = -\frac{2N \hbar\omega_0 \mathcal{V}(\beta) [1 - \mathcal{V}(\beta)] \sin(2Nx)}{[1 + \mathcal{V}(\beta)] [1 + \mathcal{V}(\beta) \cos(2Nx)]}. \quad (23)$$

These expressions make explicit how temperature enters the metrology through the monotonic visibility $\mathcal{V}(\beta)$ defined in Eq. (18). In particular, information about the interaction parameter x is suppressed when $\mathcal{V}(\beta) \rightarrow 0$ (cold, non-inverted regime $\beta \rightarrow +\infty$), because no phase is imprinted in that limit. Conversely, in the cold inverted limit $\beta \rightarrow -\infty$ one has $\mathcal{V}(\beta) \rightarrow 1$ and F_{xx} reaches its maximal Heisenberg-like scaling ($F_{xx} \sim N^2$, up to a constant factor set by our definition of x), whereas temperature information vanishes as $1 - \mathcal{V}(\beta) \rightarrow 0$. At infinite temperature ($\beta \rightarrow 0$), $\mathcal{V}(0) = 1/3$ and both $F_{\beta\beta}$ and F_{xx} remain finite.

Finally, by combining Eqs. (21)–(23) we define the scalar figure of merit

$$F_{\text{eff}}(\beta, x) = \frac{\det F(\beta, x)}{\text{Tr } F(\beta, x)}, \quad (24)$$

introduced in Sec. II, which quantifies the overall quality of the joint estimation of β and x . Maps of $F_{\text{eff}}(\beta, x)$ will be presented in Sec. V, showing the parameter regions where the estimation is most balanced between temperature and interaction strength.

D. Extension to negative temperatures

The analytical expressions above remain formally valid for negative values of the inverse temperature $\beta < 0$. In this regime the atomic population is inverted, with the excited state more populated than the ground state, corresponding to a negative absolute temperature in the conventional thermodynamic sense [91–95]. Such states can be engineered in systems with bounded spectra—for instance, spin ensembles or two-level atoms under population inversion—and have been explored in quantum thermodynamics as resources that can, in principle, deliver work against a positive-temperature bath [94–97].

As the fringe visibility adopted here, Eq. (18),

$$\mathcal{V}(\beta) = \frac{e^{-\beta\hbar\omega_0}}{2 + e^{-\beta\hbar\omega_0}}, \quad (25)$$

is *not* an odd function of β , it remains strictly positive. Negative temperatures therefore do *not* induce a π phase flip of the fringes. Instead, $\beta < 0$ enhances the contrast by increasing the population of the phase-imprinting branch $|e\rangle$. Indeed, as β crosses zero, $\mathcal{V}(\beta)$ increases from $\mathcal{V}(0) = 1/3$ to values larger than $1/3$, approaching unity in the cold inverted limit $\beta \rightarrow -\infty$.

This behavior is directly reflected in the output probabilities. Using Eq. (17),

$$P_0(\beta, x) = \frac{1 + \mathcal{V}(\beta) \cos(2Nx)}{1 + \mathcal{V}(\beta)}, \quad (26)$$

one sees that changing the sign of β changes the *amplitude* of the interference term through $\mathcal{V}(\beta)$, while the fringe phase remains fixed. In particular, the maximum remains $P_{\text{max}} = 1$, whereas the minimum $P_{\text{min}} = (1 - \mathcal{V})/(1 + \mathcal{V})$ decreases as β becomes more negative, yielding larger contrast.

The Fisher-information matrix inherits the same asymmetry. Because $\mathcal{V}(\beta)$ is monotonic and $\mathcal{V}'(\beta) = -\hbar\omega_0 \mathcal{V}(\beta) [1 - \mathcal{V}(\beta)]$, the Fisher-information elements are *not* symmetric under $\beta \rightarrow -\beta$. In fact, for our dispersive coupling (phase imprinted only for $|e\rangle$) the phase sensitivity is suppressed in the cold non-inverted limit $\beta \rightarrow +\infty$ because $\mathcal{V}(\beta) \rightarrow 0$ and no phase is imprinted, whereas it is maximized in the cold inverted limit $\beta \rightarrow -\infty$ where $\mathcal{V}(\beta) \rightarrow 1$ and the interferometer recovers the ideal NOON fringes.

In the context of quantum thermometry, negative temperatures therefore play a qualitatively different role in our scheme: they do not act by flipping the sign of the interference term, but by increasing the weight of the phase-imprinting branch, thereby enhancing the available contrast and the information about x . Conversely, the temperature sensitivity is governed by the product $\mathcal{V}(\beta) [1 - \mathcal{V}(\beta)]$ (through $\mathcal{V}'(\beta)$), which vanishes in both extreme limits $\beta \rightarrow +\infty$ and $\beta \rightarrow -\infty$ and is maximized at intermediate values of β .

From a metrological perspective, the visibility $\mathcal{V}(\beta)$ provides an operational handle on the output statistics: all entries of the Fisher information matrix can be expressed in terms of $\mathcal{V}(\beta)$ and $\mathcal{V}'(\beta)$ [Eqs. (21)–(23)]. Any process that degrades (enhances) the effective fringe contrast therefore directly diminishes (enhances) the amount of information available about the two parameters. Here we use the term *resource* in this operational sense: $\mathcal{V}(\beta)$ quantifies how strongly the thermal ancilla biases the interferometer between a phase-imprinting branch ($|e\rangle$) and a phase-free branch ($|g\rangle$), thereby controlling the metrological performance of the joint estimation of (β, x) .

This information landscape can be understood by inspecting how the parameters enter the interferometric signal. With the present coupling, x appears only in the fringe phase through $\cos(2Nx)$, whereas the inverse temperature β controls the fringe contrast through the monotonic visibility $\mathcal{V}(\beta)$. As a consequence, the phase sensitivity scales as $F_{xx} \propto \mathcal{V}(\beta)$ (up to the geometric factor $[1 + \mathcal{V}(\beta) \cos(2Nx)]^{-1}$), while the temperature sensitivity scales as $F_{\beta\beta} \propto [\mathcal{V}'(\beta)]^2$ (again up to the same geometric factor). Because $\mathcal{V}(\beta) \rightarrow 0$ for $\beta \rightarrow +\infty$ and $\mathcal{V}(\beta) \rightarrow 1$ for $\beta \rightarrow -\infty$, the device interpolates between a trivial, phase-insensitive regime at large positive β and a high-contrast phase-sensing regime at large negative β . By contrast, the optimal thermometric regime occurs at intermediate β , where $\mathcal{V}(\beta)$ is neither too small nor too close to unity, so that $|\mathcal{V}'(\beta)|$ is appreciable and the output statistics remain sensitive to changes in temperature.

IV. QUANTUM-CIRCUIT IMPLEMENTATION

In this section we show how the interferometric model of Sec. III can be mapped onto a quantum circuit acting on qubits. This provides a digital platform to simulate the joint estimation of (β, x) and to validate the analytical Fisher-information matrix derived previously. It also makes clear that the optimal measurement—photon-number detection at the output ports, effectively a two-outcome POVM—can be implemented with standard projective measurements in the computational basis.

A. Encoding of optical modes and atom

The relevant Hilbert space of the interferometer can be restricted to the two-dimensional subspace spanned

by the NOON components $|N, 0\rangle$ and $|0, N\rangle$. We encode this subspace into a single *light qubit* with logical basis

$$|0\rangle_L \equiv |N, 0\rangle, \quad |1\rangle_L \equiv |0, N\rangle. \quad (27)$$

In this encoding, the NOON state (15) becomes simply

$$|\psi_{\text{in}}\rangle = \frac{1}{\sqrt{2}}(|0\rangle_L + |1\rangle_L), \quad (28)$$

which can be prepared from $|0\rangle_L$ by a single Hadamard gate \hat{H} on the light qubit.

The two-level atom is represented by a second qubit, the *atomic qubit*, with

$$|g\rangle \equiv |0\rangle_A, \quad |e\rangle \equiv |1\rangle_A, \quad (29)$$

and Hamiltonian splitting $\hbar\omega_0$. The dispersive interaction (1) corresponds, in this effective two-qubit picture, to a controlled phase rotation on the light qubit conditioned on the atomic excitation. Up to a global phase, this can be implemented as a controlled- R_z gate

$$\hat{U}_{\text{disp}}(x) = |g\rangle\langle g| \otimes \mathbb{I}_L + |e\rangle\langle e| \otimes \hat{R}_z(2Nx), \quad (30)$$

where

$$\hat{R}_z(\phi) = e^{-i\phi\hat{\sigma}_z/2} \quad (31)$$

acts on the light qubit and generates the $2Nx$ phase difference between the logical paths. The two (nonlinear) 50:50 beam splitters of the Mach–Zehnder interferometer are represented by Hadamard gates on the light qubit, so that the overall unitary corresponding to the interferometer with dispersive interaction is

$$\hat{U}_{\text{MZI}}(x) = (\hat{H}_L \otimes \mathbb{I}_A) \hat{U}_{\text{disp}}(x) (\hat{H}_L \otimes \mathbb{I}_A). \quad (32)$$

B. Preparation of the thermal atomic state

The initial atomic state is the thermal state (14), which is diagonal in the $\{|g\rangle, |e\rangle\}$ basis. In a quantum-circuit framework, such a classical mixture can be realized in two operationally equivalent ways to realize the same reduced state:

1. *Classical sampling of initial states.* For each run of the experiment, the atomic qubit is initialized either in $|g\rangle$ or in $|e\rangle$ with probabilities

$$p_g(\beta) = \frac{1}{Z_\beta}, \quad p_e(\beta) = \frac{e^{-\beta\hbar\omega_0}}{Z_\beta}, \quad (33)$$

where Z_β is given in Eq. (14). The statistics are then obtained by averaging the measurement outcomes over many shots, weighted by these classical probabilities.

2. *Coherent preparation with an ancilla.* Alternatively, one may entangle the atomic qubit with an auxiliary qubit and then trace out the ancilla. For instance, preparing an entangled state $\sqrt{p_g} |0\rangle_{\text{anc}} |g\rangle + \sqrt{p_e} |1\rangle_{\text{anc}} |e\rangle$ and discarding the ancilla yields the desired mixed state (14) on the atom.

In our numerical simulations we adopt the second strategy.

C. Quantum circuit for the Mach–Zehnder scheme

The interferometric model of Sec. III can be implemented on a qubit-based quantum processor using the four-qubit circuit shown in Fig. 2. All qubits are initialized in the state $|0\rangle$. Qubit q_1 encodes the two-level atom, while q_2 represents the interferometer output mode that is finally measured. Qubit q_3 plays the role of the reference arm of the interferometer, and q_0 is an ancilla used to prepare the thermal state of the atom.

Thermal state preparation. The atomic thermal state $\hat{\rho}_A(\beta)$ in Eq. (14) is generated by first applying a single-qubit rotation $\hat{R}(\beta)$ to the ancilla q_0 ,

$$\hat{R}(\beta) = \begin{pmatrix} \sqrt{p_g(\beta)} & -\sqrt{p_e(\beta)} \\ \sqrt{p_e(\beta)} & \sqrt{p_g(\beta)} \end{pmatrix}, \quad (34)$$

$$p_g(\beta) = \frac{1}{1 + e^{-\beta\hbar\omega_0}}, \quad p_e(\beta) = \frac{e^{-\beta\hbar\omega_0}}{1 + e^{-\beta\hbar\omega_0}}.$$

This prepares the superposition $\hat{R}(\beta) |0\rangle_{q_0} = \sqrt{p_g} |0\rangle_{q_0} + \sqrt{p_e} |1\rangle_{q_0}$. A subsequent CNOT gate with q_0 as control and q_1 as target entangles the two qubits, encoding the classical mixture of ground and excited states in the reduced state of q_1 . Tracing out (or simply ignoring) the ancilla then leaves the atomic qubit q_1 in the desired thermal state $\hat{\rho}_A(\beta)$.

Preparation of the NOON-encoded input. The interferometer input state for $N = 1$ is the NOON-like state $(|01\rangle + |10\rangle)/\sqrt{2}$ in the two path modes. In the circuit, qubit q_3 is first flipped by an X gate, creating $|1\rangle_{q_3}$, and then a CNOT from q_3 to q_2 prepares the two-qubit state $(|01\rangle + |10\rangle)/\sqrt{2}$ in (q_2, q_3) . The first beam splitter of the Mach–Zehnder interferometer is modeled by a Hadamard gate H on q_2 , which implements the required 50:50 splitting of the optical amplitude.

Dispersive interaction and second beam splitter. The dispersive atom–field interaction of Eq. (1) is realized as a controlled phase gate between the atomic qubit q_1 and the light qubit q_2 . In the circuit this is represented by a controlled- U gate, where

$$\hat{U}(x) = \begin{pmatrix} 1 & 0 \\ 0 & e^{-ix} \end{pmatrix}, \quad (35)$$

acts on q_2 whenever q_1 is in the excited state $|1\rangle$, ensuring that only one arm of the interferometer acquires

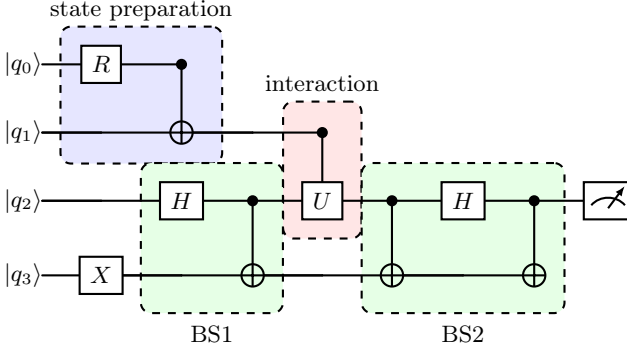


FIG. 2. Quantum circuit used to simulate the Mach-Zehnder interferometer for $N = 1$. Qubit q_1 encodes the thermal two-level atom, q_2 represents the interferometer output mode that is measured, and q_3 corresponds to the reference arm. Qubit q_0 is an ancilla used to prepare the atomic thermal state via the rotation R and a CNOT. The dispersive interaction is implemented as a controlled- U gate between q_1 and q_2 , while Hadamard and CNOT gates model the beam splitters.

the dispersive phase x . The second beam splitter of the Mach-Zehnder interferometer is then modeled by a final CNOT gate with q_2 as control and q_3 as target, followed by a Hadamard gate on q_2 and another CNOT gate in the same configuration as the first one.

Measurement and statistics. At the end of the circuit the light qubit q_2 is measured in the computational basis, yielding a classical bit c_0 that records whether the photons exit through the reference port ($|0\rangle_{q_2}$) or the complementary port ($|1\rangle_{q_2}$). Repeating the circuit for many shots and for different pairs (β, x) reconstructs the probabilities $P_0(\beta, x)$ and $P_1(\beta, x)$, which, as discussed in Secs. III and V, agree with the analytical prediction of Eq. (17) and allow us to estimate the entries of the Fisher-information matrix.

D. Measurement and reconstruction of the Fisher information

The measurement stage consists of projective measurements in the computational basis of the light qubit, which correspond to detecting whether the photons exit through one output port ($|0\rangle_L$) or the other ($|1\rangle_L$). Since the atomic state is not measured, the full POVM is given by

$$\hat{\Pi}_0 = |0\rangle_L\langle 0| \otimes \mathbb{I}_A, \quad \hat{\Pi}_N = |1\rangle_L\langle 1| \otimes \mathbb{I}_A, \quad (36)$$

which reproduces the probabilities $P_0(\beta, x)$ and $P_N(\beta, x)$ in Eq. (17). Importantly, the POVM elements do not depend on (β, x) , and the output state is always diagonal in the measurement basis. As a result, the eigenvectors of $\hat{\rho}(\beta, x)$ are parameter-independent, and the classical Fisher-information matrix associated with this POVM coincides with the QFIM:

$$F(\beta, x) = Q(\beta, x). \quad (37)$$

Therefore, the simple computational-basis measurement implemented in the circuit is already optimal and saturates the quantum multiparameter Cramér–Rao bound.

From the circuit, for each chosen pair (β, x) we obtain empirical frequencies

$$\hat{P}_0(\beta, x) = \frac{n_0}{\mu}, \quad \hat{P}_N(\beta, x) = \frac{n_N}{\mu}, \quad (38)$$

where n_0 and n_N are the counts of outcomes 0 and N in μ shots. These frequencies converge, for large μ , to the theoretical probabilities P_0 and P_N in Eq. (17). The classical Fisher-information matrix is then estimated by inserting the empirical probabilities into Eq. (20). In practice, we use the analytical derivatives (19) evaluated at (β, x) together with the empirical \hat{P}_0 and \hat{P}_N , so that the only source of discrepancy between F and its estimate \hat{F} comes from sampling noise.

E. Simulation details and comparison with analytical results

The full protocol can be summarized as follows:

1. Choose a grid of parameter values (β, x) of interest.
2. For each grid point:
 - (a) Prepare the thermal atomic state $\rho_A(\beta)$ using the ancilla-assisted circuit described in Sec. IV, i.e., by applying the appropriate single-qubit rotation on the ancilla and a CNOT to entangle it with the atomic qubit, followed by tracing out (or discarding) the ancilla.
 - (b) Prepare the NOON-encoded state $(|0\rangle_L + |1\rangle_L)/\sqrt{2}$ on the light qubit.
 - (c) Apply the interferometric unitary $\hat{U}_{\text{MZI}}(x)$ in Eq. (32).
 - (d) Measure the light qubit in the computational basis and record the outcome.
 - (e) Repeat steps (a)–(d) a total of μ times to obtain the empirical probabilities \hat{P}_0 and \hat{P}_N .
3. Use Eq. (20) together with Eq. (19) to reconstruct the Fisher-information matrix elements $\hat{F}_{\beta\beta}$, \hat{F}_{xx} and $\hat{F}_{\beta x}$.

In Sec. V we compare the numerically reconstructed Fisher-information matrix \hat{F} with the analytical expressions (21)–(23) derived from the visibility-based model. We find excellent agreement across the parameter space, with deviations fully accounted for by finite-sampling fluctuations. This confirms that the quantum circuit faithfully reproduces the interferometric dynamics and that the simple computational-basis measurement is sufficient to attain the optimal precision limits for the joint estimation of temperature and interaction strength.

V. RESULTS AND DISCUSSION

A. Validation of the interferometric statistics

We first compare the numerically simulated interference probabilities obtained from the quantum circuit with the analytical prediction of Eq. (17). Figure 3 shows the three-dimensional surfaces of $P_0(\beta, x)$ from the circuit simulation [panel (a)] and from the analytical model [panel (b)]. The two plots are indistinguishable within the statistical fluctuations associated with the finite number of shots ($\mu = 10^4$ in our runs). As β decreases (increasing inversion), the contrast increases: minima become deeper while the maxima remain fixed at $P_{\max} = 1$. The high degree of agreement between simulation and theory validates the digital representation of the Mach-Zehnder interferometer introduced in Sec. IV.

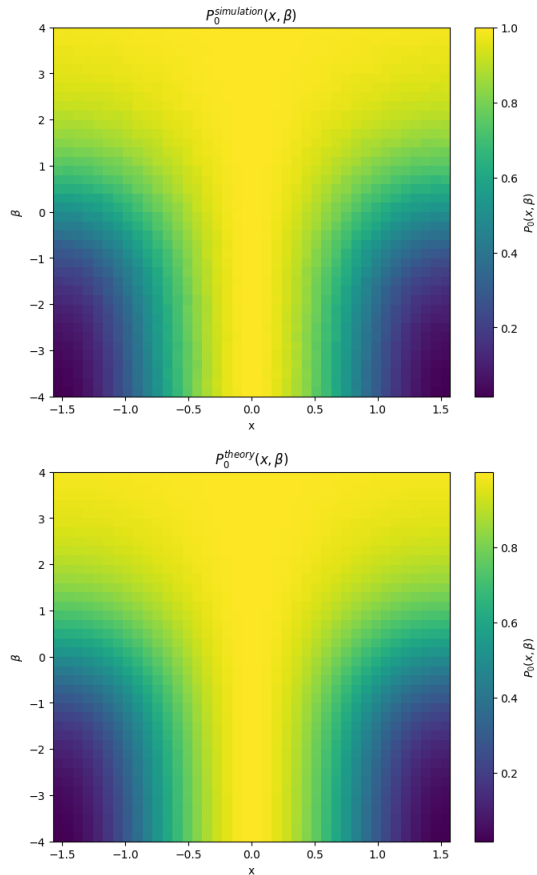


FIG. 3. Comparison between simulated and analytical interference probabilities. (a) Simulation results $P_0(\beta, x)$ obtained from 10^4 circuit shots. (b) Analytical prediction from Eq. (17). The color scale encodes the probability of detecting all photons at the reference output port.

B. Information landscape from the analytical QFIM

We now turn to the quantum Fisher-information matrix. The element $Q_{xx}(\beta, x)$ quantifies the ultimate precision with which the dispersive phase x can be estimated when β is unknown. Figure 4 displays Q_{xx} as a function of (β, x) for NOON probes with $N = 1$ [panel (a)] and $N = 10$ [panel (b)]. In both cases the phase information is *suppressed* for large positive β (cold non-inverted regime), because $\mathcal{V}(\beta) \rightarrow 0$ and the atom remains in $|g\rangle$ so that no phase is imprinted. As β decreases and the excited population grows, $\mathcal{V}(\beta)$ increases and the phase information rises, reaching its maximal value $Q_{xx}^{\max} \simeq 4N^2$ in the cold inverted limit $\beta \rightarrow -\infty$, where $\mathcal{V}(\beta) \rightarrow 1$ and the interferometer recovers the ideal NOON fringes. At $\beta=0$, the visibility is finite, $\mathcal{V}(0) = 1/3$, and Q_{xx} remains finite (albeit reduced compared to the inverted regime). Increasing N enhances the overall scale of Q_{xx} by approximately a factor N^2 and produces narrower interference fringes along x , giving rise to several equivalent operating points separated by π/N .

The complementary element $Q_{\beta\beta}(\beta, x)$ encodes the sensitivity to temperature (or, more precisely, to the inverse temperature β). Its landscape is shown in Fig. 5 for $N = 1$ [panel (a)] and $N = 10$ [panel (b)]. In contrast with Q_{xx} , the thermal information is concentrated in an intermediate band of β , where the visibility changes most rapidly. Since $\mathcal{V}'(\beta) = -\hbar\omega_0 \mathcal{V}(\beta)[1 - \mathcal{V}(\beta)]$, the strongest thermometric response occurs when $\mathcal{V}(\beta)$ is neither too small nor too close to unity (roughly around $\mathcal{V} \sim 1/2$, i.e., $\beta\hbar\omega_0 \approx -\ln 2$). For large $|\beta|$ the atom becomes nearly pure (ground for $\beta \rightarrow +\infty$ or excited for $\beta \rightarrow -\infty$), and $Q_{\beta\beta}$ is suppressed. The overall magnitude of $Q_{\beta\beta}$ remains of order unity and is essentially independent of N , reflecting that temperature information is encoded in the single-atom thermal visibility, while the NOON super-resolution mainly boosts phase sensitivity. For $N = 10$ the thermal information is modulated by multiple narrow fringes along x , aligned with the phase-sensitive lobes of Q_{xx} .

To characterize the relative importance of phase and temperature estimation, we define the fraction

$$f_x(\beta, x) = \frac{Q_{xx}(\beta, x)}{Q_{\beta\beta}(\beta, x) + Q_{xx}(\beta, x)}, \quad (39)$$

which ranges from 0 (purely thermometric regime) to 1 (purely phase-sensitive regime). Figure 6 shows $f_x(\beta, x)$ for NOON probes with $N = 1$ [panel (a)] and $N = 10$ [panel (b)]. For $N = 1$, the interferometer behaves predominantly as a phase sensor in the inverted regime (more negative β), while an intermediate band of β exists where $Q_{\beta\beta}$ becomes comparable to Q_{xx} and the device effectively acts as a thermometer. For $N = 10$ the phase sensitivity is further enhanced: f_x is close to unity over a broad region of the (β, x) plane, and the pronounced thermometric regions appear as thin horizontal stripes

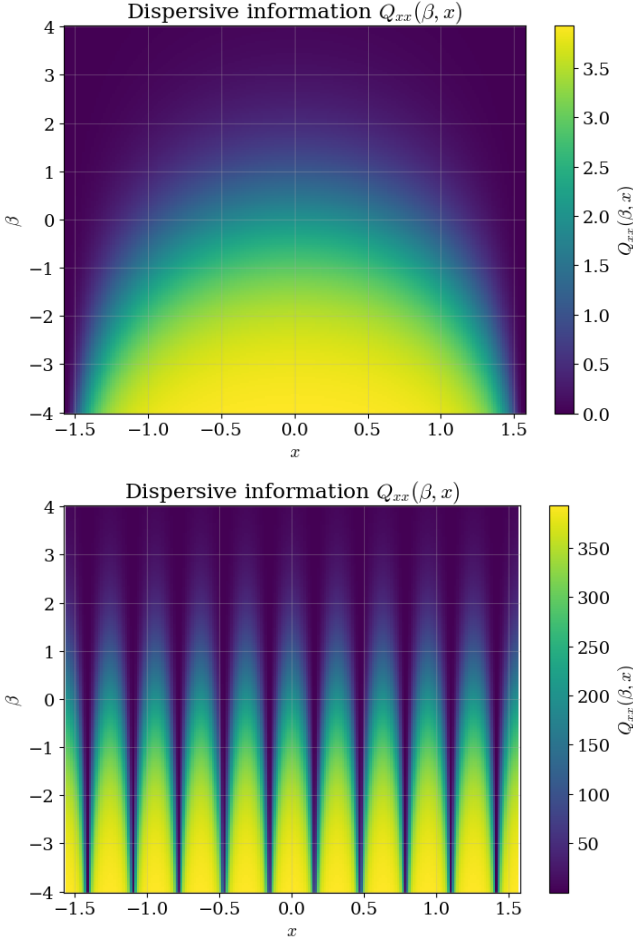


FIG. 4. Dispersive information $Q_{xx}(\beta, x)$ as a function of inverse temperature and interaction strength for NOON probes with (a) $N = 1$ and (b) $N = 10$ photons. The information is suppressed for large positive β (cold non-inverted regime, $\mathcal{V} \rightarrow 0$), and it approaches its maximum $Q_{xx}^{\max} \simeq 4N^2$ in the cold inverted limit $\beta \rightarrow -\infty$ where $\mathcal{V} \rightarrow 1$. At $\beta = 0$ one has $\mathcal{V}(0) = 1/3$, so Q_{xx} remains finite. Increasing N enhances the maximal information approximately as N^2 and produces narrower interference fringes along x , leading to multiple equivalent operating points.

at phase values where Q_{xx} is suppressed by destructive interference.

The total information available from the output statistics is given by the trace of the QFIM,

$$\mathcal{I}(\beta, x) = \text{Tr}[Q(\beta, x)] = Q_{\beta\beta}(\beta, x) + Q_{xx}(\beta, x). \quad (40)$$

Figure 7 displays $\mathcal{I}(\beta, x)$ as a function of (β, x) for NOON probes with $N = 1$ [panel (a)] and $N = 10$ [panel (b)]. For $N = 1$ the information is maximal in regions where the fringe slope is large and the visibility is appreciable, typically on the negative- β side where the excited branch is significantly populated. The black contour marks the region where $\mathcal{I}(\beta, x) \geq (1 - \delta)\mathcal{I}_{\max}$ with $\delta = 0.05$, thus identifying an almost-optimal plateau of operating points that retain at least 95% of the maximal information. For

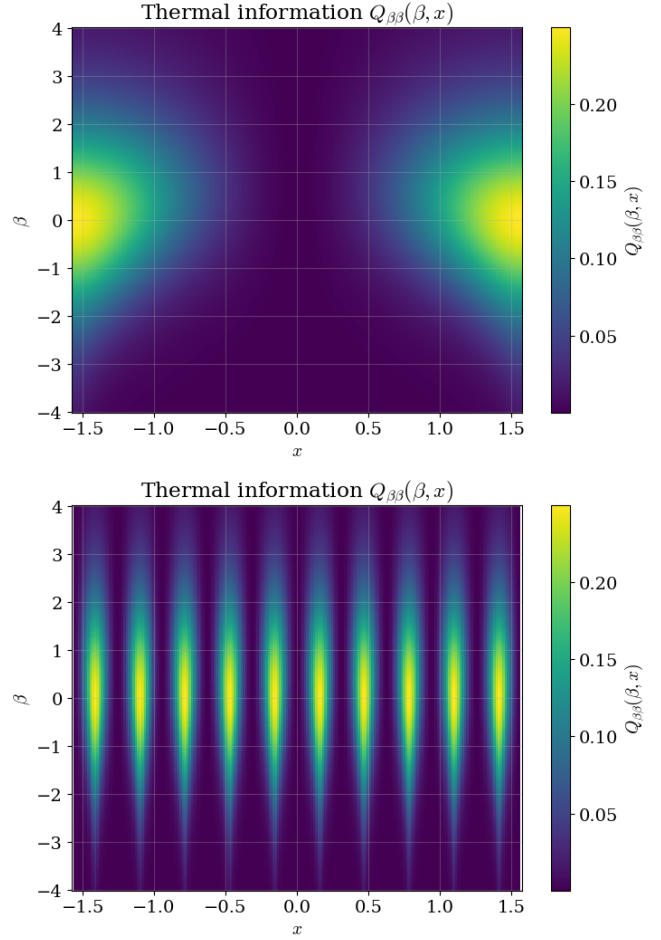


FIG. 5. Thermal information $Q_{\beta\beta}(\beta, x)$ for NOON probes with (a) $N = 1$ and (b) $N = 10$ photons. The information is concentrated in an intermediate β band where the visibility varies most rapidly (i.e., where $|\mathcal{V}'(\beta)|$ is largest), and it is suppressed for $|\beta| \rightarrow \infty$ where the atom becomes nearly pure. The overall scale of $Q_{\beta\beta}$ is essentially independent of N , while larger N produces a fine fringe structure along x that mirrors the phase-sensitive lobes of Q_{xx} .

$N = 10$ the landscape is dominated by a sequence of narrow lobes along x , inherited from the super-resolved interference fringes of Q_{xx} . The overall scale of \mathcal{I} grows approximately as N^2 , and several equivalent optimal operating points appear, one at the center of each high-visibility lobe, as highlighted by the black contour.

C. Benchmarking the QFIM with circuit simulations

To benchmark the quantum-circuit implementation, we compare the Fisher information extracted from the simulated statistics with the analytical prediction for a representative off-diagonal element of the QFIM. Figure 8 shows the color map of the cross Fisher information $Q_{\beta x}(\beta, x)$ obtained from the circuit (top) and from the

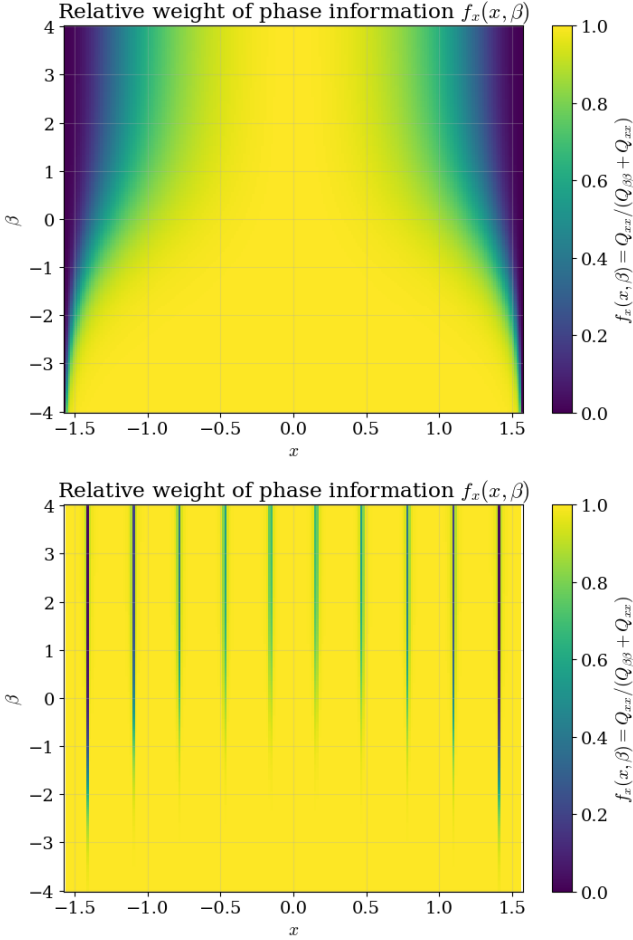


FIG. 6. Relative weight of phase information $f_x(\beta, x) = Q_{xx}/(Q_{\beta\beta} + Q_{xx})$ for NOON probes with (a) $N = 1$ and (b) $N = 10$ photons. Yellow regions ($f_x \simeq 1$) correspond to regimes dominated by dispersive-phase estimation, most prominently in the inverted (negative- β) sector where the visibility is high. Darker regions highlight thermometric bands where $Q_{\beta\beta}$ becomes comparable to Q_{xx} .

analytical formula (bottom). The agreement is excellent over the whole parameter region considered: both the magnitude and the shape of the surface are faithfully reproduced by the simulation. Small discrepancies at the edges of the domain are consistent with finite-sampling fluctuations due to the large imbalance between the two outcomes when P_0 is very close to 0 or 1.

For completeness, we have also computed analogous surfaces for the diagonal elements Q_{xx} and $Q_{\beta\beta}$. They display the same level of agreement between simulation and theory as in Fig. 8 and are therefore not shown here.

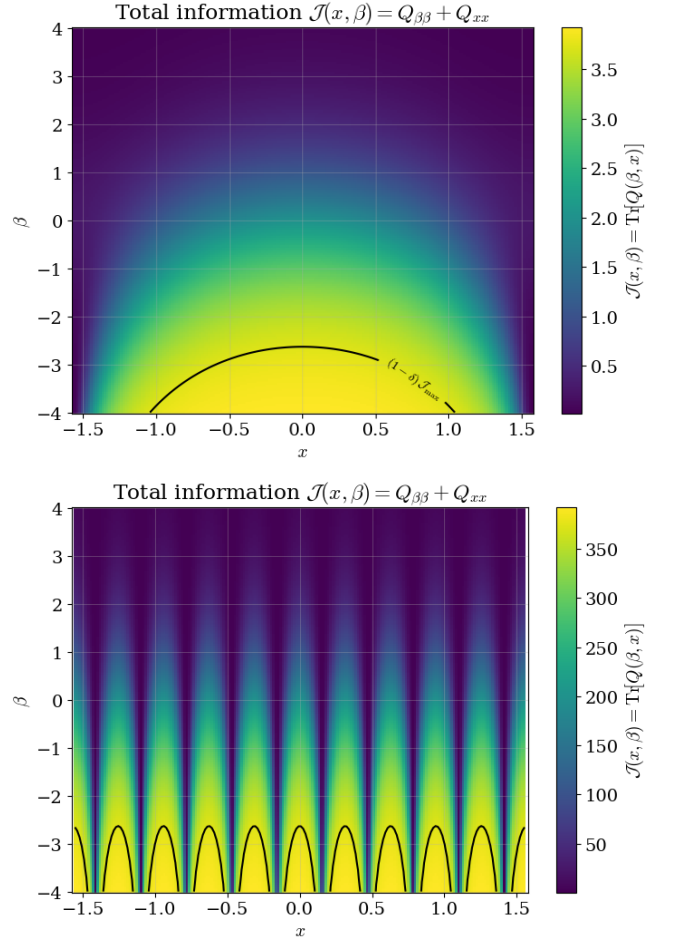


FIG. 7. Total information $\mathcal{I}(\beta, x) = Q_{\beta\beta}(\beta, x) + Q_{xx}(\beta, x)$ for NOON probes with (a) $N = 1$ and (b) $N = 10$ photons. In panel (a) the black contour encloses the region where $\mathcal{I} \geq (1 - \delta) \mathcal{I}_{\max}$ with $\delta = 0.05$, corresponding to an almost-optimal plateau of operating points that retain at least 95% of the maximal information. For $N = 10$ [panel (b)] the information scale is enhanced roughly as N^2 and multiple equivalent optimal operating points emerge along x , one in each interference lobe, as indicated by the black contour.

D. Experimental validation on IBM Quantum hardware

To complement the analytical and simulation benchmarks reported above, we executed the quantum circuit of Fig. 2 on an IBM Quantum device, thereby providing a proof-of-principle experimental validation of the joint-estimation protocol and of the reconstructed Fisher-information landscape under realistic noise and finite sampling. For these hardware runs, we executed the transpiled circuits on the IBM Quantum backend `ibm_torino`, using $\mu = 10000$ shots per grid point. Circuits were transpiled with Qiskit at optimization level 1, and no error-mitigation procedures were applied.

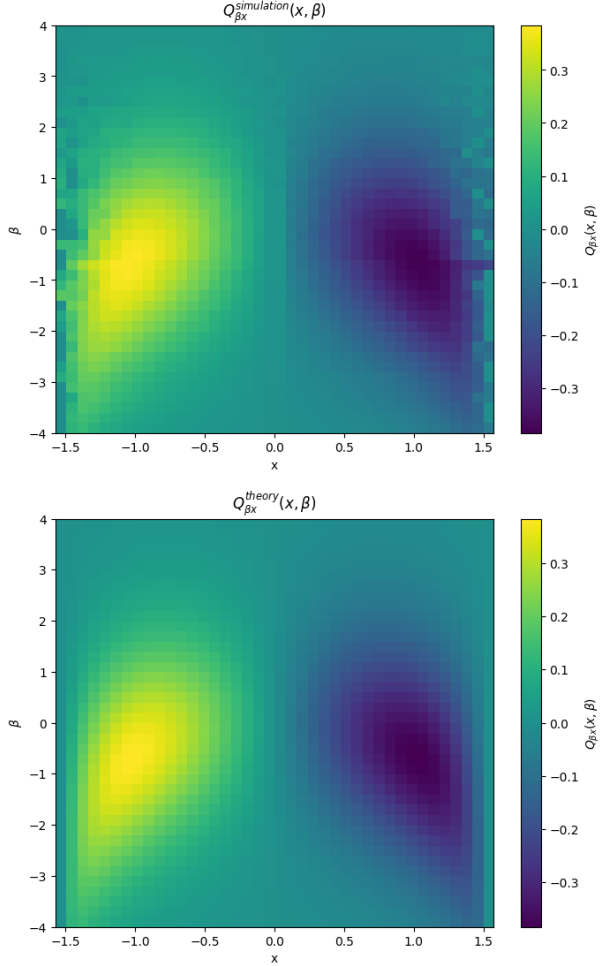


FIG. 8. Cross Fisher information $Q_{\beta x}(\beta, x)$ from circuit simulation (top) and from the analytical expression (bottom). The two 3D surfaces coincide within statistical fluctuations, confirming that the digital implementation reproduces the continuous interferometric model and its joint-dependence on (β, x) .

a. Hardware execution and data acquisition. For each point of a 20×20 grid in (β, x) with $\beta \in [-4, 4]$ and $x \in [-\pi/2, \pi/2]$ (uniformly spaced), we compiled the four-qubit circuit of Fig. 2 to the native gate set of the chosen IBM backend. The measurement consists of a projective readout of the light qubit (encoding the interferometer output port) in the computational basis. From the raw counts n_0 and n_1 , we estimate the empirical frequency $\hat{P}_0(\beta, x) = n_0/\mu$, which converges to the ideal probability $P_0(\beta, x)$ in the limit of large μ . In practice, device noise and finite sampling reduce the fringe contrast and introduce small asymmetries across the parameter domain.

b. Reconstruction of the Fisher-information matrix. Given the two-outcome statistics, the (classical) Fisher-information matrix elements are reconstructed using the same strategy adopted for the circuit simulations: we use the analytical derivatives of $P_0(\beta, x)$ and substitute

the exact probabilities with the experimental frequencies \hat{P}_0 . This yields an experimentally reconstructed matrix $\hat{F}(\beta, x)$ with entries $\hat{F}_{\beta\beta}$, \hat{F}_{xx} , and $\hat{F}_{\beta x}$.

c. Experimental landscapes. Figure 9 summarizes the experimentally reconstructed surfaces. Panel (a) shows the measured interference probability $\hat{P}_0(\beta, x)$, which retains the expected periodic dependence along x but with visibly reduced contrast compared to the ideal prediction, consistent with a noise-induced reduction of the effective visibility. Here “visibility” in the hardware data refers to the same operational contrast $V_{\text{meas}} \equiv (P_{\text{max}} - P_{\text{min}})/(P_{\text{max}} + P_{\text{min}})$ extracted from $\hat{P}_0(\beta, x)$; in the unitary limit $V_{\text{meas}} = V(\beta)$ [Eq. (18)], while device noise and SPAM errors reduce it ($V_{\text{meas}} < V$), explaining the suppressed magnitudes in Fig. 9. Panels (b)–(d) show the reconstructed Fisher-information entries. Despite the reduced absolute magnitudes, the experiment reproduces the main qualitative features discussed in Sec. V: (i) $\hat{F}_{\beta\beta}$ is concentrated in the intermediate region where the visibility changes most rapidly with β ; (ii) \hat{F}_{xx} is largest in regions where the fringe slope is maximal; and (iii) the cross term $\hat{F}_{\beta x}$ changes sign across $x = 0$, reflecting the odd symmetry associated with $\partial_x P_0 \propto \sin(2Nx)$.

d. Error Analysis and Systematic Bias. Error bars for the reconstructed Fisher information elements \hat{F}_{ij} were estimated via bootstrap resampling of the experimental shot counts, yielding relative uncertainties $\sigma_F/F \approx 1/\sqrt{\mu}$. We emphasize that the experimental surfaces in Fig. 9 represent raw data without any error mitigation or noise fitting. To interpret the deviations, we inferred point estimates $(\hat{\beta}, \hat{x})$ from the fringe data (Table I). We observe a systematic bias consistent with a *contrast shrinkage* mechanism: the measured fringe visibility is pulled toward a baseline value close to $V(0) = 1/3$ (infinite-temperature reference), i.e.,

$$V_{\text{meas}} \simeq \kappa V(\beta_{\text{true}}) + (1 - \kappa) V(0), \quad 0 < \kappa < 1, \quad (41)$$

which is a generic effective model for SPAM errors and unmitigated decoherence that partially randomize the output statistics. Since the estimator $\hat{\beta} = V^{-1}(V_{\text{meas}})$ is constructed by inverting the monotonic visibility map (Appendix C), this shrinkage biases the estimate toward $\beta \simeq 0$, yielding $|\hat{\beta}| < |\beta_{\text{true}}|$ for both signs of β . This provides an operational signature of the dominant noise channels, which act primarily by degrading the effective fringe contrast (see Appendix C).

E. Interpretation and physical implications

The combined analytical and numerical results confirm that the interferometer acts as a dual probe: it can function as a high-precision phase sensor in the *inverted* ($-\beta$) regime or as a thermometer in an intermediate band of β where the visibility varies most rapidly. For large negative β , the atomic ancilla is almost pure in the excited state, the visibility approaches unity, and

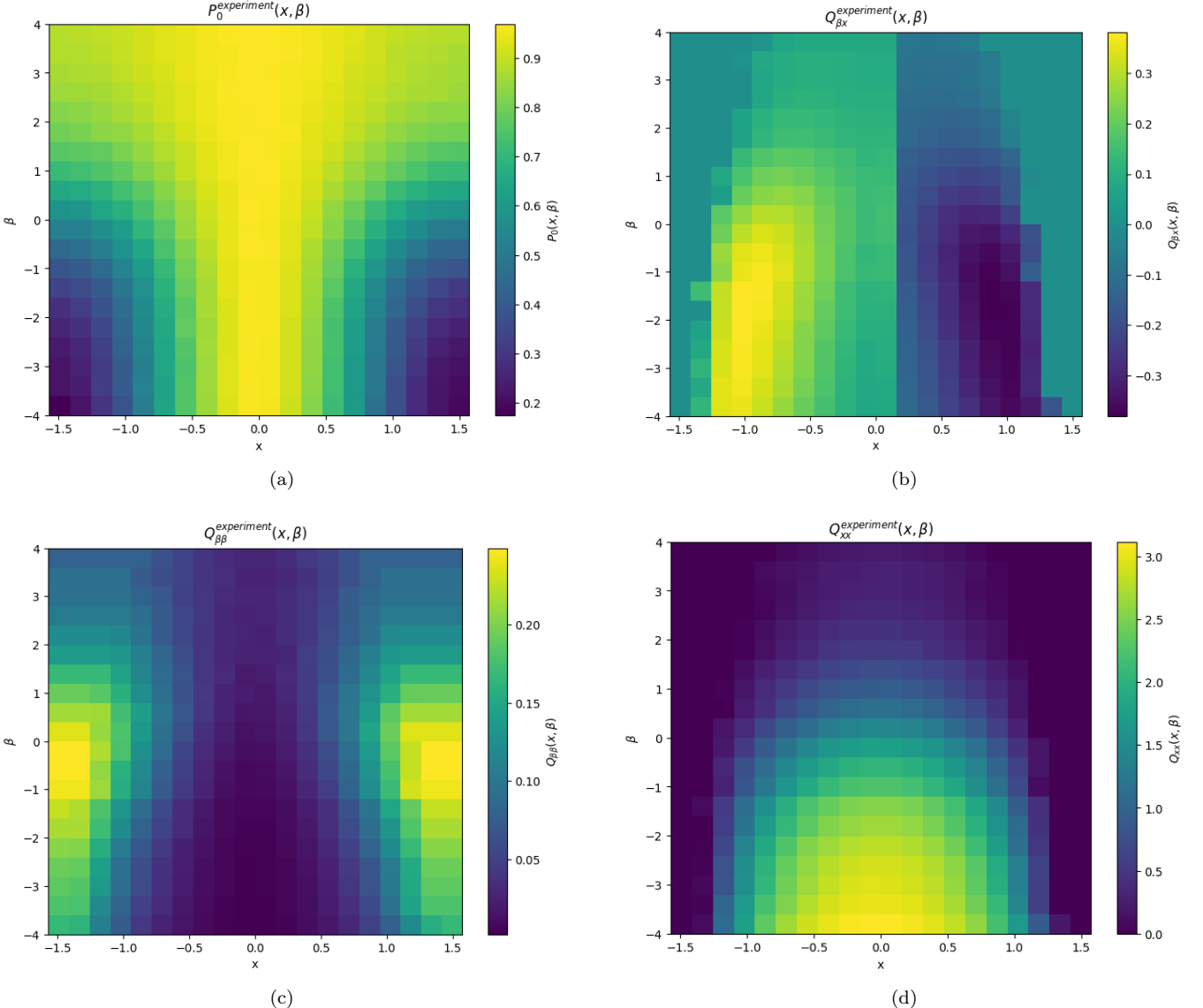


FIG. 9. Experimental reconstruction on IBM Quantum hardware. (a) Measured interference probability $\hat{P}_0(\beta, x)$. (b) Reconstructed cross term $\hat{F}_{\beta x}(\beta, x)$. (c) Reconstructed Fisher information $\hat{F}_{\beta\beta}(\beta, x)$. (d) Reconstructed Fisher information $\hat{F}_{xx}(\beta, x)$. The experiment captures the qualitative structure of the ideal information landscape, while device noise reduces the fringe contrast and hence suppresses the overall magnitudes.

the phase information Q_{xx} dominates with Heisenberg-like scaling in N . For large positive β , the ancilla is almost pure in the ground state, $\mathcal{V}(\beta) \rightarrow 0$, and both Q_{xx} and $Q_{\beta\beta}$ are suppressed because no dispersive phase is imprinted and the output statistics become nearly deterministic ($P_0 \rightarrow 1$). For intermediate β , thermal mixing makes $|\mathcal{V}'(\beta)|$ appreciable, leading to enhanced temperature sensitivity encoded in $Q_{\beta\beta}$. Thus, the same interferometric architecture can operate in distinct metrological modes, governed by the single control parameter β through $\mathcal{V}(\beta)$.

F. Tuning and Inverted Populations

a. Resonance Tuning (ω_0). The trade-off between thermometer and phase-sensor regimes is governed by the energy scale $\hbar\omega_0$. The temperature sensitivity peaks when the visibility slope is maximal, i.e., when β is such that $\mathcal{V}(\beta)[1 - \mathcal{V}(\beta)]$ is appreciable. Consequently, the sensor is tunable: by adjusting the atomic splitting ω_0 (e.g., via Zeeman or Stark shifts), one can shift the effective *thermometer window* to the target temperature range. We note that inhomogeneous broadening (a distribution of ω_0 across an ensemble) would act as an additional dephasing channel, averaging out $\mathcal{V}(\beta)$ and re-

TABLE I. Representative experimental points (IBM hardware) and corresponding ideal-simulator values. Values extracted from the 20×20 grid used to build Fig. 9.

β	x	$\hat{\beta}_{\text{exp}}$	\hat{x}_{exp}	$\hat{P}_{0,\text{exp}}$	$\hat{\beta}_{\text{sim}}$	\hat{x}_{sim}	$\hat{P}_{0,\text{sim}}$
-4.0	$-\pi/2$	-1.308	-1.571	0.175	-3.842	-1.571	0.017
-4.0	-0.083	-1.308	-0.222	0.962	-3.842	-0.085	0.993
-4.0	$+\pi/2$	-1.308	1.571	0.193	-3.842	1.570	0.021
0.211	$-\pi/2$	0.467	-1.571	0.584	0.084	-1.331	0.548
0.211	-0.083	0.467	-0.299	0.966	0.084	-0.046	0.999
0.211	$+\pi/2$	0.467	1.571	0.581	0.084	1.571	0.520
4.0	$-\pi/2$	2.345	-1.571	0.88	3.749	-1.565	0.977
4.0	-0.083	2.345	-0.657	0.967	3.749	0.000	1.000
4.0	$+\pi/2$	2.345	1.571	0.88	3.749	1.271	0.979

ducing the peak Fisher information.

b. Negative Temperatures. Our analysis extends naturally to negative temperatures ($\beta < 0$), relevant for population-inverted systems. Experimentally, such states can be prepared in the thermal ancilla by engineered inversion protocols (e.g., a high-fidelity π -pulse applied to an initially equilibrated two-level system, followed by controlled mixing). Within our operational definition, inversion corresponds to $\mathcal{V}(\beta) > \mathcal{V}(0) = 1/3$, and it manifests as an enhancement of fringe contrast (deeper minima) rather than as a π phase flip. The cross-correlation term $F_{\beta x}$ changes sign across $x = 0$ because it is proportional to $\sin(2Nx)$, while its β -dependence is governed by the monotonic factor $\mathcal{V}(\beta)[1 - \mathcal{V}(\beta)]$. Hence, the metrological signature of inversion in this model is encoded in the *contrast level* (and thus in \mathcal{V}), not in an antisymmetry under $\beta \rightarrow -\beta$.

VI. ROBUSTNESS ANALYSIS AND EXPERIMENTAL LIMITATIONS

The transition from idealized quantum metrology to practical sensing is defined by the *Multiparameter Frontier*, where the simultaneous estimation of signal and noise parameters becomes unavoidable. While the model in Sec. III relies on a clean trade-off governed by thermal visibility $\mathcal{V}(\beta)$, realistic sensors operate in open environments where decoherence is not merely a scalar reduction in contrast, but a dynamical process that fundamentally reshapes the statistical manifold. In this section, we move beyond the unitary limit to rigorously assess the protocol's robustness under joint Amplitude Damping (AD) and Phase Damping (PD)—the two dominant noise channels in quantum hardware. By adopting the recently developed framework of *Fisher Information Susceptibility* χ_F [88], we quantify the fragility of different probe states, establishing a metrological hierarchy that guides platform-specific implementation. Furthermore, this theoretical analysis provides the necessary physical context to interpret the systematic deviations and bias

observed in our experimental validation (Sec. V D).

A. Decoherence Models and Noise Hierarchy

In any physical realization of the MZI, the probe experiences simultaneous energy relaxation (amplitude damping) and dephasing (phase damping). We model this non-unitary evolution via the Lindblad master equation [98]:

$$\frac{d\rho}{dt} = -i[\hat{H}(\theta), \rho] + \gamma_{\text{AD}} \mathcal{D}[\hat{a}]\rho + \gamma_{\text{PD}} \mathcal{D}[\hat{a}^\dagger \hat{a}]\rho, \quad (42)$$

where $\mathcal{D}[\hat{L}]\rho = \hat{L}\rho\hat{L}^\dagger - \frac{1}{2}\{\hat{L}^\dagger\hat{L}, \rho\}$ is the standard dissipator. To map these continuous-time dynamics onto the discrete parameter space of our results (Fig. 10), we define the dimensionless *transmission efficiency* η and *dephasing strength* γ as:

$$\eta \equiv e^{-\gamma_{\text{AD}}t}, \quad \gamma \equiv \frac{\gamma_{\text{PD}}t}{2}, \quad (43)$$

where t is the total interaction time. Physically, η represents the probability that a single photon survives the passage through the interferometer arms (where $1 - \eta$ is the loss probability), while γ sets the accumulated phase-diffusion variance in the NOON coherence.

Under these channels, the ideal thermal visibility $\mathcal{V}(\beta)$ derived in Eq. (18) degrades into an effective visibility \mathcal{V}_{eff} . For an N -photon NOON state, which requires the coherence of the maximally separated Fock superposition, this degradation scales as (see Appendix A for the explicit derivation from the Lindblad dynamics):

$$\mathcal{V}_{\text{eff}}(\beta, \eta, \gamma) = \eta^{N/2} e^{-\gamma N^2} \mathcal{V}(\beta). \quad (44)$$

Note that the scaling with N highlights the extreme susceptibility of this state: the term $e^{-\gamma N^2}$ reflects the quadratic enhancement of phase noise sensitivity, while $\eta^{N/2}$ (or η^N for coincidence detection) captures the exponential probability of avoiding photon loss. This definition of η provides the rigorous physical basis for the x-axis in Fig. 10, allowing us to directly correlate the dynamical decay rates with the metrological performance limits.

B. Metrological Hierarchy Under Joint Noise

To quantify the impact of these channels, we evaluate the robustness of three distinct probe classes currently dominant in the literature. By analyzing the Fisher Information surfaces in Fig. 10 and the incompatibility maps in Fig. 11, we reveal a hierarchy determined by the structural response to photon loss.

NOON States: The Fragile Benchmark. While NOON states theoretically achieve the Heisenberg limit ($F_{xx} \propto N^2$), this advantage is strictly confined to a noise-free manifold. As visualized in the top row of Fig. 10,

the effective Fisher information F_{eff} exhibits a dramatic *cliff-edge* collapse, rendering the state useless for transmission efficiencies $\eta < 0.95$. This behavior is rigorously explained by the Fisher Information Susceptibility derived in Appendix B, which proves that the metrological fragility scales cubically ($\chi_F \propto N^3$) under amplitude damping. Consequently, for any $\gamma > 0$, the rapid contraction of the useful parameter space confirms that high- N NOON states are inferior to classical strategies in realistic open systems [99, 100]. (See Appendix B 4 for a detailed reconciliation of these susceptibility scalings with the asymptotic bounds of Escher et al. [101].)

Squeezed Vacuum: Gaussian Resilience. In stark contrast, Two-Mode Squeezed Vacuum (TMSV) states maintain their Gaussian character under amplitude damping. This resilience is strikingly evident in the bottom row of Fig. 10, where the region of high F_{eff} (bright area) extends significantly further into the lossy regime ($\eta \sim 0.7$) compared to NOON states. Because photon loss acts as a diffusive process that degrades the squeezing parameter $r \rightarrow r'$ without destroying entanglement [102], TMSV states serve as a *robust workhorse* for steady-state sensing. However, this robustness comes at a cost. As shown in Fig. 11(c), squeezed states exhibit a persistent *ridge* of high statistical incompatibility $\mathcal{I}_{\beta x}$ in the low-noise regime. This implies that while the information survives, extracting it requires optimal, non-Gaussian measurements that are distinct for temperature and phase, complicating the readout strategy compared to the simple photon counting used for NOON states [50, 103].

Cat States: The Non-Gaussian Compromise. Schrödinger Cat states ($|\psi_{\text{cat}}\rangle \propto |\alpha\rangle + |-\alpha\rangle$) occupy a strategic middle ground. The middle row of Fig. 10 confirms that they withstand amplitude damping better than NOON states, avoiding the sudden death of coherence. This structural robustness arises because a single photon loss event induces a parity flip ($|\text{even}\rangle \rightarrow |\text{odd}\rangle$) rather than a collapse to a mixture, preserving the quantum superposition. Furthermore, Fig. 11(b) indicates that Cat states maintain lower incompatibility $\mathcal{I}_{\beta x}$ than squeezed states in the relevant operating regions. Thus, Cat states offer a compelling compromise: they retain significant Quantum Fisher Information in transient, lossy regimes (unlike NOON states) while potentially easing the measurement burden (unlike Squeezed states) via parity-based detection schemes [104, 105]. For a rigorous derivation of the susceptibility scaling for Cat and Squeezed states, and their comparison to the NOON limit, see Appendix D.

C. Joint Discussion: Robustness vs. Incompatibility

The interplay between the Fisher information landscapes (Fig. 10) and the statistical incompatibility (Fig. 11) reveals a fundamental resource trade-off.

Figure 10 establishes a clear hierarchy of structural robustness. The NOON state acts as a fragile *glass cannon*: its advantage is strictly confined to a vanishingly small corner of the parameter space ($\eta \approx 1$). The rapid decay of F_{eff} confirms that any significant photon loss catastrophically destroys the coherence resource $\mathcal{V}(\beta)$. In contrast, the Squeezed state exhibits a broad, robust plateau in F_{eff} , maintaining metrological utility even down to efficiencies of $\eta \sim 0.7$. This resilience stems from the continuous-variable nature of Gaussian entanglement, which degrades algebraically rather than exponentially under loss.

However, Figure 11 adds a critical nuance. Robustness does not imply ease of access. The Squeezed state exhibits significant statistical incompatibility $\mathcal{I}_{\beta x}$ (Fig. 11c), particularly in the high-efficiency regimes. This non-vanishing commutator implies that the optimal measurements for temperature ($\hat{\Pi}_\beta$) and phase ($\hat{\Pi}_x$) do not commute. Consequently, experimentally realizing the theoretical limit requires advanced readout schemes, such as general dyne detection, to navigate this uncertainty trade-off.

Conversely, the NOON state's incompatibility vanishes rapidly as noise increases (Fig. 11a), but this is a trivial consequence of the state decohering into a classical mixture. The Cat state emerges as a compelling intermediate candidate, offering higher peak sensitivity than the Squeezed state in transient regimes while possessing a non-Gaussian structure that mitigates the incompatibility cost via information backflow.

D. Platform-Specific Implementation Constraints

The theoretical models derived above provide a direct explanation for the experimental behaviors observed in different hardware implementations.

1. Circuit QED (Superconducting Qubits)

The microwave resonator serves as the MZI arms, and the transmon qubit serves as the thermal ancilla $\hat{\rho}_A(\beta)$.

- **Justification for the $N = 1$ Limit:** Our experimental validation on `ibm_torino` was deliberately restricted to the single-qubit probe limit ($N = 1$). This choice is informed by the scaling analysis in Ref. [79], which showed that the coherence of a NOON state under phase damping decays super-exponentially as $\exp(-\gamma N^2 t)$. By operating at $N = 1$, we avoid this *cliff-edge* decoherence regime, allowing us to isolate and quantify the systematic bias introduced solely by Amplitude Damping (photon loss/relaxation). As observed in Table I and detailed in Appendix C, this manifests as a contraction of the Bloch vector that the estimator misinterprets as a thermal mixing (a *hotter* state).

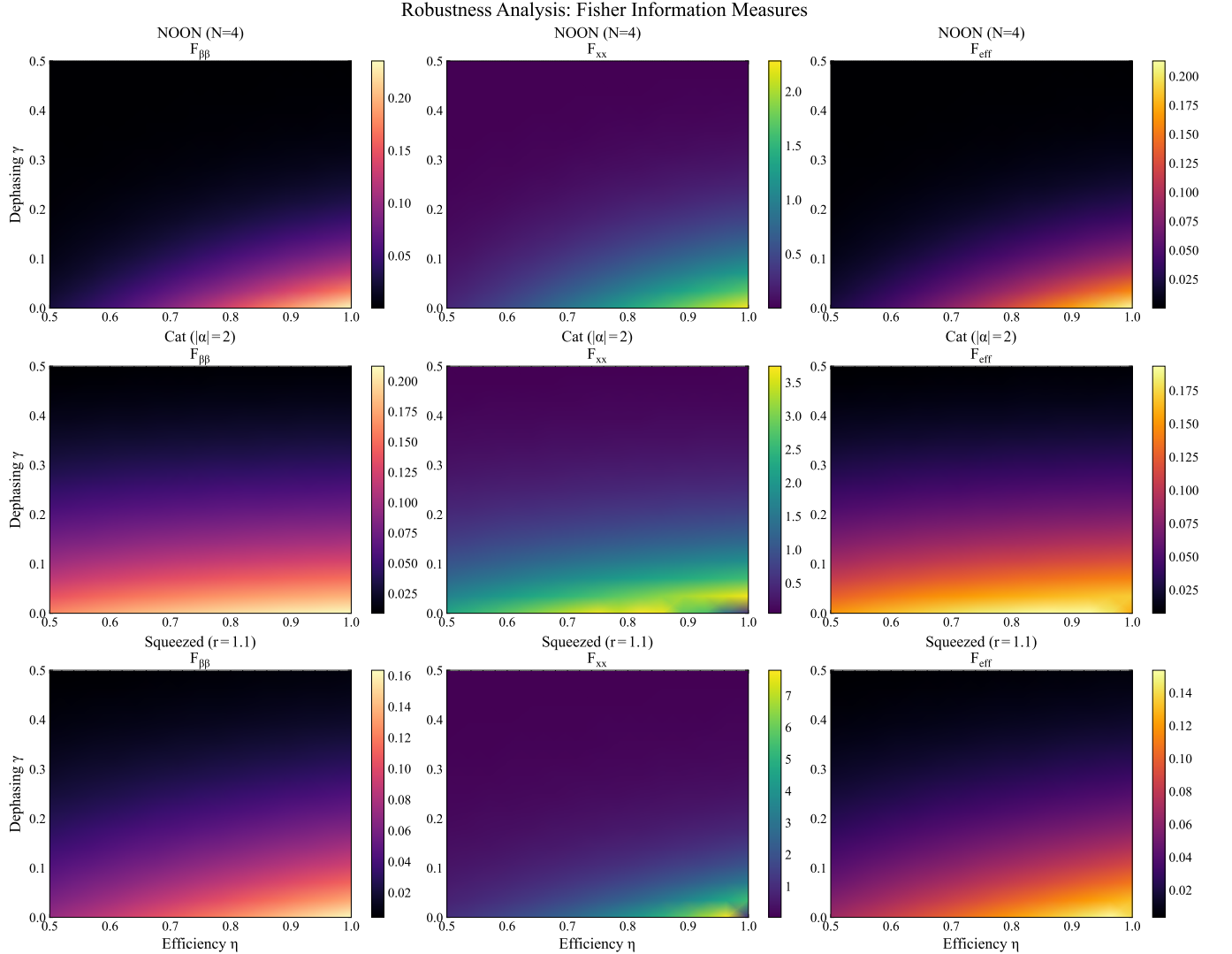


FIG. 10. **Decoherence Landscape and Robustness Hierarchy.** Evaluation of the Quantum Fisher Information (QFI) elements $F_{\beta\beta}$ (temperature, left column), F_{xx} (phase, middle column), and the effective joint information F_{eff} (right column) for NOON ($N = 4$), Cat ($|\alpha| = 2$), and Squeezed ($r = 1.1$) states. The performance is mapped across the parameter space of transmission efficiency η (x-axis) and dephasing rate γ (y-axis), evaluated at the representative operating point $\beta = 0.5$ and $x = \pi/4$. (Top Row) **NOON States** show maximal peak sensitivity but exhibit a *cliff-edge* collapse, rendering them useless for $\eta < 0.95$. (Middle Row) **Cat States** offer a non-Gaussian compromise with broader resilience. (Bottom Row) **Squeezed States** demonstrate superior global robustness, maintaining a high F_{eff} (bright region) over a significantly larger area of the noise landscape, confirming their status as the preferred probe for realistic open systems.

- **Optimal Regime:** Despite the T_2 (γ_{PD}) limitations, this platform remains ideal for the *transient thermometry* protocols discussed in Ref. [79]. Since the optimal interaction time t_{opt} scales inversely with the coupling strength χ , strong dispersive coupling allows for parameter estimation on timescales shorter than the rapid N^2 -enhanced dephasing, provided that readout error mitigation is applied.

2. Integrated Quantum Photonics

Waveguides implement the MZI paths with high propagation loss ($\alpha \sim 0.1 - 3$ dB/cm) [106].

- **Constraint:** Unlike cQED, the limitation here is transmission η .
- **Recommendation:** Squeezed states are preferred, maintaining a quantum advantage down to $\eta \sim 0.7$, whereas the NOON-based visibility \mathcal{V}_{eff} vanishes rapidly [107].

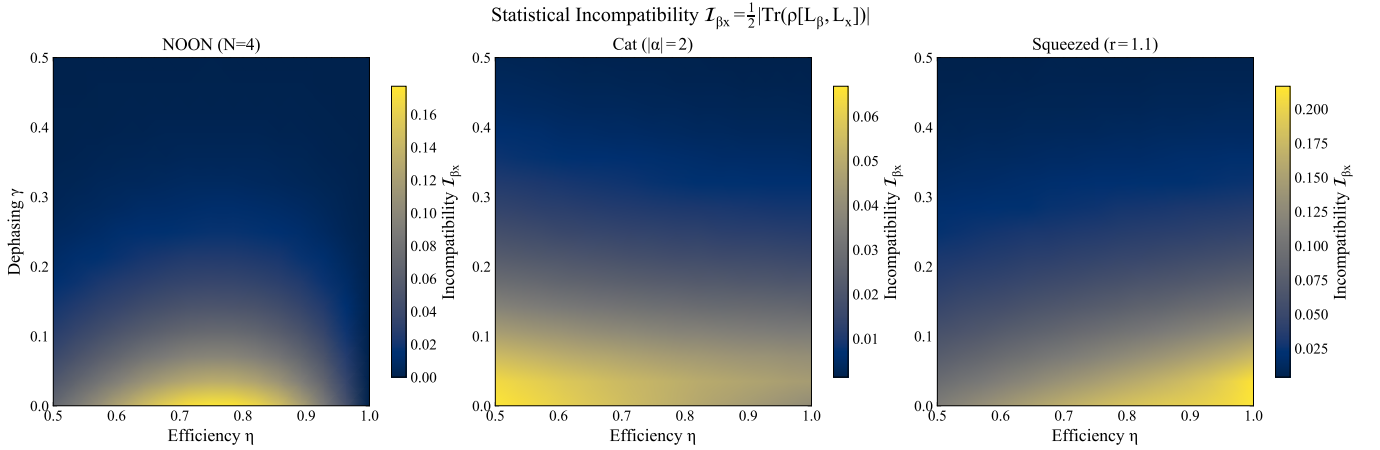


FIG. 11. **Statistical Incompatibility $\mathcal{I}_{\beta x}$.** The magnitude of the commutator expectation value $\mathcal{I}_{\beta x} = \frac{1}{2}|\text{Tr}(\rho[L_\beta, L_x])|$ for (a) NOON, (b) Cat, and (c) Squeezed states under joint amplitude and phase damping. Brighter regions indicate higher incompatibility, implying a stricter Heisenberg uncertainty trade-off that forbids the simultaneous saturation of the Cramér-Rao bounds for temperature and phase. Notably, **Squeezed States** (c) retain a *ridge* of high incompatibility in the low-noise regime, indicating that their robustness comes at the cost of required optimal simultaneous measurements.

3. Trapped Ion Platforms

The MZI modes a and b are mapped to collective motional modes (phonons) via Raman laser pulses [108].

- **Motional Heating:** The environment adds phonons at a rate \dot{n} [109], acting as a significant AD channel that destroys NOON interference $P_0(\beta, x)$.
- **Dicke Alternative:** Symmetric Dicke states $|N/2, N/2\rangle_S$ are increasingly preferred for dispersive sensing due to their robustness against the local phase noise (γ) common in Paul traps [110].

E. Error Mitigation and Resource Optimization

To extend the protocol's operational range and reclaim the metrological advantage in the presence of noise, several high-level mitigation strategies must be integrated into the control layer:

- **Adaptive Preparation:** Real-time feedback allows the experimentalist to match state parameters—such as the squeezing degree r —to the transient noise levels [111].
- **Dynamical Decoupling:** Sequences like spin-echo in superconducting circuits can suppress ancilla dephasing, extending the effective coherence time T_2 by an order of magnitude [112, 113].
- **Bayesian Inference:** Treating noise parameters (η, γ) as nuisance variables within a joint estimation model allows for self-calibration. This would effectively correct the AD-induced bias observed in our IBM experiment [114].

- **Variational Compilation:** Variational algorithms can *learn* structured entanglement inherently tailored to the specific noise eigenstructure of the channel [115].

F. Extensions and Future Directions

The analysis of robustness under joint damping reveals several promising research frontiers that bridge fundamental metrology with condensed matter physics. One such avenue is the utilization of *Discrete Time Crystals* (DTCs) as robust probes for periodic-field sensing [116]. Unlike static superpositions, the inherent phase rigidity of a DTC locks the sensing signal to a sub-harmonic of the drive frequency, providing a natural shield against the phase fluctuations (γ) that typically limit Ramsey-type interferometry.

Additionally, the extension of this protocol to distributed quantum networks suggests a paradigm for spatial temperature mapping and field sensing across non-local nodes [117, 118]. In such configurations, the robustness of Squeezed and Dicke states becomes the primary enabling factor for maintaining networked entanglement over lossy communication channels. Ultimately, these developments suggest that the optimal probe for noisy environments may not be a simple quantum state, but a dynamical phase of matter or an error-corrected logical qubit specifically engineered to survive the Multiparameter Frontier.

VII. CONCLUSIONS AND OUTLOOK

We have investigated a scheme for quantum multiparameter estimation, utilizing a Mach-Zehnder interfer-

ometer coupled to a thermal two-level atom to jointly estimate the inverse temperature β and the dispersive interaction parameter x . Our analysis establishes that the atomic ancilla acts as a tunable resource, modulating the interferometric signal through a temperature-dependent visibility $\mathcal{V}(\beta)$ defined operationally from the output fringes. By deriving closed analytical expressions for the Quantum Fisher Information Matrix (QFIM), we demonstrated that all metrological bounds are saturable via simple photon-number measurements, as the output state remains diagonal in a parameter-independent basis. The resulting information landscape reveals a distinct duality: the device behaves predominantly as a Heisenberg-like phase sensor in the cold inverted regime ($\beta \rightarrow -\infty$, where $\mathcal{V} \rightarrow 1$) and as a high-sensitivity thermometer in an intermediate band of β where $|\mathcal{V}'(\beta)|$ is maximal, while it becomes nearly trivial in the cold non-inverted limit ($\beta \rightarrow +\infty$, where $\mathcal{V} \rightarrow 0$ and $P_0 \rightarrow 1$).

Extending this framework to open quantum systems, we identified a *Multiparameter Frontier* where the simultaneous presence of Amplitude Damping (AD) and Phase Damping (PD) fundamentally reshapes the estimation limits. Our robustness analysis, quantified by the Fisher Information Susceptibility χ_F , established a clear metrological hierarchy: while NOON states offer maximal peak sensitivity, they act as *glass cannons* that shatter under minimal loss ($\eta < 0.95$). In contrast, Squeezed Vacuum states emerged as the robust standard for steady-state sensing, albeit with a non-trivial statistical incompatibility $\mathcal{I}_{\beta x}$ that necessitates optimal simultaneous measurements. We further highlighted standard Cat states as a promising intermediate candidate, capable of exploiting information backflow for transient thermometry by retaining coherence through parity encoding.

To validate these predictions, we mapped the protocol to a qubit-based circuit and executed it on the `ibm_torino` quantum processor. The experimental reconstruction of the Fisher information landscape successfully reproduced the key qualitative features of the ideal model. Crucially, the observed systematic bias in the temperature estimator is consistent with an effective contrast shrinkage mechanism that pulls the measured visibility toward a baseline close to $\mathcal{V}(0) = 1/3$. In the simplest phenomenological description this can be captured by an affine model $\mathcal{V}_{\text{meas}} \simeq \kappa \mathcal{V}(\beta) + (1 - \kappa) \mathcal{V}(0)$, which biases $\hat{\beta} = \mathcal{V}^{-1}(\mathcal{V}_{\text{meas}})$ toward $\beta \simeq 0$ (Appendix C). This proof-of-principle demonstration confirms that current NISQ devices can already serve as testbeds for observing the subtle trade-offs inherent to multiparameter metrology.

Looking forward, this work opens several avenues for research at the intersection of metrology and condensed matter physics. On the theoretical front, the integration of *Discrete Time Crystals* (DTCs) offers a pathway to bypass the dephasing limits of static probes by exploiting phase rigidity for periodic-field sensing. Similarly, extending the protocol to distributed quantum networks could enable the simultaneous mapping of spa-

tial temperature gradients and non-local field correlations. On the practical side, the implementation of error-mitigation strategies—specifically Bayesian inference for self-calibration (including nuisance parameters that control contrast loss) and variational compilation for noise-adapted state preparation—will be essential to transition from qualitative demonstration to near-optimal precision in realistic environments. Ultimately, our results illustrate that visibility engineering is not merely a descriptive tool, but a potent design principle for the next generation of tunable, multiparameter quantum sensors.

Appendix A: Derivation of Effective Visibility under Joint Damping

This appendix derives the effective visibility \mathcal{V}_{eff} used in Sec. VI A, starting from the Lindblad master equation that describes the optical mode's evolution under simultaneous amplitude and phase damping.

1. Master equation and coherence evolution

The evolution of the probe state's density matrix $\hat{\rho}$ is governed by the standard Lindblad master equation [98]:

$$\frac{d\hat{\rho}}{dt} = \gamma_{\text{AD}} \mathcal{D}[\hat{a}](\hat{\rho}) + \gamma_{\text{PD}} \mathcal{D}[\hat{n}](\hat{\rho}), \quad (\text{A1})$$

where γ_{AD} and γ_{PD} are the amplitude and phase damping rates, respectively, and $\mathcal{D}[\hat{L}](\hat{\rho}) = \hat{L}\hat{\rho}\hat{L}^\dagger - \frac{1}{2}\{\hat{L}^\dagger\hat{L}, \hat{\rho}\}$. Here, \hat{a} is the annihilation operator and $\hat{n} = \hat{a}^\dagger\hat{a}$ is the number operator.

For a coherence element $\rho_{nm}(t) = \langle n|\hat{\rho}(t)|m\rangle$ in the Fock basis, the diagonal ($n = m$) and off-diagonal ($n \neq m$) elements evolve independently. The differential equation for an off-diagonal element is:

$$\frac{d\rho_{nm}}{dt} = - \left[\frac{\gamma_{\text{AD}}}{2}(n+m) + \frac{\gamma_{\text{PD}}}{2}(n-m)^2 \right] \rho_{nm}. \quad (\text{A2})$$

2. Application to NOON-state coherence

Consider a NOON state $|\psi\rangle = (|N,0\rangle + |0,N\rangle)/\sqrt{2}$ in the two-mode representation. After the interferometer, the relevant coherence that determines fringe visibility is the term $\rho_{N0}(t) = \langle N|\hat{\rho}_{\text{out}}(t)|0\rangle$. Setting $n = N$ and $m = 0$ in the above equation yields:

$$\frac{d\rho_{N0}}{dt} = - \left[\frac{\gamma_{\text{AD}}N}{2} + \frac{\gamma_{\text{PD}}N^2}{2} \right] \rho_{N0}. \quad (\text{A3})$$

The solution is an exponential decay in time:

$$\rho_{N0}(t) = \rho_{N0}(0) \exp \left(-\frac{\gamma_{\text{AD}}Nt}{2} - \frac{\gamma_{\text{PD}}N^2t}{2} \right). \quad (\text{A4})$$

3. Effective visibility with thermal ancilla

Defining the dimensionless transmission efficiency $\eta = e^{-\gamma_{\text{AD}} t}$ and the dephasing strength $\gamma = \gamma_{\text{PDT}}/2$, the coherence factor becomes $D_N = \eta^{N/2} e^{-\gamma N^2}$. When the interferometer includes a thermal ancilla with inverse temperature β , the ideal (unitary) fringe visibility is the operational quantity $\mathcal{V}(\beta)$ defined in Eq. (18). The damping channels multiply this ideal visibility by the coherence factor D_N , yielding the effective visibility:

$$\mathcal{V}_{\text{eff}}(\beta, \eta, \gamma) = \eta^{N/2} e^{-\gamma N^2} \mathcal{V}(\beta). \quad (\text{A5})$$

This result highlights the distinct scaling behaviors: amplitude damping causes an exponential decay $\propto \eta^{N/2}$, while phase damping causes a super-exponential decay $\propto e^{-\gamma N^2}$. The quadratic scaling with N in the phase-damping exponent underpins the extreme fragility of NOON states to dephasing noise discussed in Sec. VI.

Appendix B: Fisher Information Susceptibility and Scaling Laws

To strictly quantify the *Glass Cannon* hierarchy, we derive the Fisher Information Susceptibility (χ_F) for NOON states under local amplitude damping and phase diffusion, and reconcile these local derivatives with the global asymptotic bounds of Escher et al. [101].

1. Definition of Susceptibility

The Fisher Information Susceptibility χ_F measures the leading-order degradation of the Quantum Fisher Information (QFI) under a weak noise channel \mathcal{E}_ϵ characterized by a small parameter ϵ [88]:

$$F(\epsilon) = F(0) - \epsilon \chi_F + O(\epsilon^2). \quad (\text{B1})$$

2. Susceptibility to Amplitude Damping (Photon Loss)

Consider the NOON state $|\psi\rangle = (|N, 0\rangle + |0, N\rangle)/\sqrt{2}$. Under single-photon loss with probability ϵ (transmission $\eta = 1 - \epsilon$), the state evolves into a mixture. Crucially, the loss of a single photon from mode a projects the state to $|N-1, 0\rangle$, which is orthogonal to the original superposition. The survival probability of the coherence is $P_{\text{surv}} = (1 - \epsilon)^N \approx 1 - N\epsilon$.

The effective visibility scales as $\mathcal{V}_{\text{eff}} \approx 1 - N\epsilon$. Since the QFI for phase estimation scales as $F_Q \propto N^2 \mathcal{V}_{\text{eff}}^2$, expanding to first order yields:

$$F_Q(\epsilon) \approx N^2 (1 - N\epsilon)^2 \approx N^2 - 2N^3\epsilon. \quad (\text{B2})$$

Identifying terms, we find the susceptibility to amplitude damping scales cubically:

$$\chi_{\text{AD}} \propto N^3. \quad (\text{B3})$$

This confirms that the relative fragility $\chi_F/F(0) \propto N$ grows linearly with photon number.

3. Susceptibility to Dephasing

The scaling of dephasing depends on the correlation of the noise. For *Global Dephasing* (collective fluctuations), the generator $\hat{L} = \hat{n}_a + \hat{n}_b = \hat{N}$ commutes with the NOON state, causing no decoherence. For *Differential Dephasing* (the relevant metrological noise), the generator is $\hat{L} = \hat{n}_a - \hat{n}_b$. The variance of this generator for a NOON state is $\langle (\Delta \hat{L})^2 \rangle = N^2$. The off-diagonal elements decay as $e^{-\frac{1}{2}\epsilon N^2}$. Following the expansion $F_Q \propto N^2 (e^{-\frac{1}{2}\epsilon N^2})^2 \approx N^2 (1 - \epsilon N^2)$, we obtain:

$$F_Q(\epsilon) \approx N^2 - N^4 \epsilon \implies \chi_{\text{PD}} \propto N^4. \quad (\text{B4})$$

Thus, NOON states are polynomially more fragile to phase diffusion ($\chi \propto N^4$) than to loss ($\chi \propto N^3$). However, in standard hardware, ϵ_{AD} often dominates ϵ_{PD} .

4. Bridging Susceptibility and Asymptotic Bounds

Finally, we map our local susceptibility metric onto the global asymptotic bounds established by Escher et al. [101] and Demkowicz-Dobrzański et al. [119]. The Escher bound for lossy interferometry dictates that precision is bounded by the Standard Quantum Limit scaling, $\Delta\phi \geq \frac{\sqrt{1-\eta}}{2\sqrt{\eta N}}$, implying that Heisenberg scaling ($1/N$) is transient.

The susceptibility χ_F essentially defines the *duration* of this transient regime. We define a *Critical Photon Number* N_{crit} where the noise-induced reduction becomes comparable to the initial quantum advantage:

$$N^2 \sim \epsilon \cdot \chi_F(N). \quad (\text{B5})$$

Substituting our derived susceptibility for loss, $\chi_{\text{AD}} \propto N^3$, we recover:

$$N^2 \sim \epsilon N^3 \implies N_{\text{crit}} \sim \frac{1}{\epsilon}. \quad (\text{B6})$$

This matches the known breakdown point of NOON states. For $N < N_{\text{crit}}$, the state operates in the *Glass Cannon* regime where quantum advantage is possible. For $N > N_{\text{crit}}$, the cubic susceptibility overwhelms the quadratic gain. In contrast, Squeezed Vacuum states possess a susceptibility structure that allows them to saturate the Escher bound asymptotically, maintaining a constant factor advantage over the SQL even for large N . Our metrological hierarchy is thus a ranking of N_{crit} for different probe architectures.

Appendix C: Theoretical Model of Experimental Bias

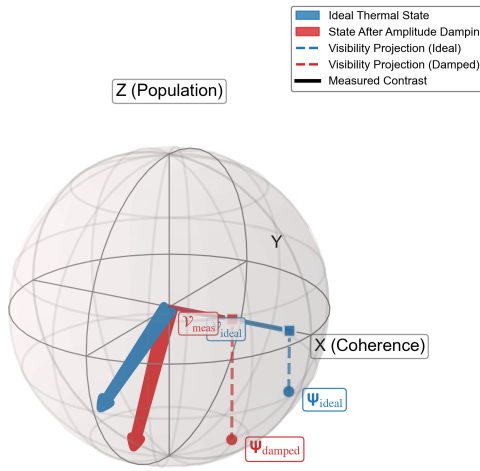


FIG. 12. Schematic visualization of a contrast-shrinkage bias mechanism. Unmitigated noise channels and SPAM errors effectively reduce the observed fringe contrast, pulling the inferred visibility toward a baseline close to $\mathcal{V}(0) = 1/3$. When β is estimated by inverting the monotonic map $\mathcal{V}(\beta)$, this shrinkage biases $\hat{\beta}$ toward $\beta \simeq 0$, yielding $|\hat{\beta}| < |\beta_{\text{true}}|$ over broad operating regions.

This appendix provides an analytical model for the systematic bias observed in the experimental temperature estimates (Sec. V D), where $\hat{\beta}_{\text{exp}}$ underestimates the true magnitude $|\beta_{\text{true}}|$. In the present framework, β is inferred operationally through the fringe visibility $\mathcal{V}(\beta)$ defined from the output probabilities.

1. Estimator construction and inverse map

From Eq. (18), the visibility is

$$\mathcal{V}(\beta) = \frac{e^{-\beta\hbar\omega_0}}{2 + e^{-\beta\hbar\omega_0}}, \quad 0 < \mathcal{V} < 1. \quad (\text{C1})$$

Inverting this monotonic map yields the estimator

$$\hat{\beta} = \mathcal{V}^{-1}(\mathcal{V}_{\text{meas}}) = -\frac{1}{\hbar\omega_0} \ln\left(\frac{2\mathcal{V}_{\text{meas}}}{1 - \mathcal{V}_{\text{meas}}}\right). \quad (\text{C2})$$

Operationally, $\mathcal{V}_{\text{meas}}$ can be obtained either directly from the measured extrema of $P_0(\beta, x)$ (e.g., via P_{max} and P_{min}) or by fitting a fringe model to P_0 versus x at fixed β .

2. Contrast shrinkage and bias toward $\beta \simeq 0$

A minimal phenomenological description of unmitigated decoherence and SPAM errors is that they partially

randomize the output statistics, reducing contrast and pulling the effective visibility toward a baseline. Since $\mathcal{V}(0) = 1/3$ plays the role of the infinite-temperature reference point in the ideal model, we model

$$\mathcal{V}_{\text{meas}} \simeq \kappa \mathcal{V}(\beta_{\text{true}}) + (1 - \kappa) \mathcal{V}(0), \quad 0 < \kappa < 1. \quad (\text{C3})$$

This affine shrinkage has two key consequences: (i) if $\beta_{\text{true}} > 0$ then $\mathcal{V}(\beta_{\text{true}}) < 1/3$, so Eq. (C3) increases the observed visibility; (ii) if $\beta_{\text{true}} < 0$ then $\mathcal{V}(\beta_{\text{true}}) > 1/3$, so Eq. (C3) decreases it. In both cases, $\mathcal{V}_{\text{meas}}$ is moved closer to $1/3$, and therefore $\hat{\beta}$ obtained from Eq. (C2) is biased toward 0, i.e.,

$$|\hat{\beta}| < |\beta_{\text{true}}| \quad (\text{C4})$$

over a broad range of parameters (consistent with the trends in Table I).

3. Correction protocol

If κ can be independently calibrated (e.g., by preparing reference points with known β or by dedicated process tomography), then an unbiased estimate can be obtained by undoing the shrinkage:

$$\hat{\beta}_{\text{corr}} = \mathcal{V}^{-1}\left(\frac{\mathcal{V}_{\text{meas}} - (1 - \kappa)\mathcal{V}(0)}{\kappa}\right), \quad (\text{C5})$$

provided the argument lies in $(0, 1)$. Alternatively, in a multiparameter inference one may treat κ as a nuisance parameter and jointly fit (β, κ) from the same fringe data, trading additional statistical uncertainty for immunity to systematic bias.

Appendix D: Comparative Metrological Hierarchy

This appendix provides a rigorous analytical foundation for the metrological hierarchy presented in Fig. 10, extending the susceptibility analysis of Appendix B to Schrödinger Cat and Squeezed Vacuum states. We quantify their relative robustness under amplitude damping and explain their distinct operational regimes.

1. Schrödinger Cat States: Non-Gaussian Resilience

Consider the even-parity cat state $|\psi_{\text{cat}}\rangle = \mathcal{N}(|\alpha\rangle + |-\alpha\rangle)$, where $\mathcal{N} = [2(1 + e^{-2|\alpha|^2})]^{-1/2}$ and the mean photon number is $\bar{n} \approx |\alpha|^2$ for $|\alpha| \gg 1$. Unlike NOON states, photon loss does not immediately destroy quantum coherence but rather induces a parity flip: $\hat{a}|\text{even}\rangle \rightarrow \alpha|\text{odd}\rangle$. This preserves the macroscopic superposition, merely rotating it in phase space.

TABLE II. Metrological hierarchy of quantum probe states. The susceptibility χ_F quantifies the linear degradation of QFI under weak amplitude damping, while the robustness index \mathcal{R} measures the preserved fraction at $\epsilon = 0.1$.

Probe State	Ideal QFI (F_0)	Susceptibility (χ_F)	Scaling	Robustness $\mathcal{R}(\epsilon = 0.1)$
NOON State	$\sim N^2$	$\sim N^3$	Exponential collapse	< 0.01 (Fragile)
Cat State	$\sim \bar{n}^2$	$\sim \bar{n}^3$	Exponential decay	$\sim e^{-0.4\bar{n}}$ (Conditional)
Squeezed Vacuum	$\sim \bar{n}^2$ (lossless) $\sim \bar{n}$ (lossy)	$\sim \bar{n}$	Graceful degradation	~ 0.9 (Optimal)

The off-diagonal coherence element $\langle \alpha | -\alpha \rangle = e^{-2|\alpha|^2}$ decays under amplitude damping with transmission η as:

$$\mathcal{C}_{\text{cat}}(\eta) \approx \exp[-2|\alpha|^2(1 - \sqrt{\eta})]. \quad (\text{D1})$$

For weak loss ($\eta = 1 - \epsilon$, $\epsilon \ll 1$), this becomes $\mathcal{C}_{\text{cat}} \approx e^{-2\bar{n}\epsilon}$. The quantum Fisher information for parameter θ encoded via a unitary $\hat{U}_\theta = e^{i\theta\hat{n}}$ consequently scales as:

$$F_{\text{cat}}(\theta) \approx 4\bar{n}^2 e^{-4\bar{n}\epsilon}. \quad (\text{D2})$$

The Fisher Information Susceptibility therefore scales as:

$$\chi_F^{(\text{cat})} \propto \bar{n}^3 e^{-4\bar{n}\epsilon} \Big|_{\epsilon \rightarrow 0} \sim \bar{n}^3. \quad (\text{D3})$$

Despite this cubic scaling, cat states maintain Heisenberg-limited sensitivity ($F \propto \bar{n}^2$) until $\epsilon \sim 1/\bar{n}$. This contrasts sharply with NOON states, which fail catastrophically at $\epsilon \sim 1/N$. The critical advantage is that cat states retain phase sensitivity even after multiple photon losses, provided the parity-flipped state remains coherent. This makes them particularly suitable for *transient thermometry* where non-Markovian information backflow can be harnessed [105].

2. Squeezed Vacuum States: Gaussian Optimality

The two-mode squeezed vacuum (TMSV) state $|\xi\rangle = \hat{S}_{12}(\xi)|0,0\rangle$, with squeezing parameter r ($\xi = re^{i\phi}$) and mean photon number per mode $\bar{n} = \sinh^2 r$, represents the optimal Gaussian probe. Under amplitude damping, the state remains Gaussian, with the covariance matrix transforming linearly. The quantum Fisher information for phase estimation in a lossy Mach-Zehnder interferometer with transmission η is given by the exact expression [101]:

$$F_{\text{SQ}}(x) = \frac{\eta(\bar{n}^2 + \bar{n})}{1 - \eta + \frac{1}{2\bar{n} + 1}}. \quad (\text{D4})$$

In the high-squeezing limit ($\bar{n} \gg 1$), this simplifies to:

$$F_{\text{SQ}}(x) \approx \frac{\eta\bar{n}}{1 - \eta} \quad \text{for fixed } \eta < 1. \quad (\text{D5})$$

This demonstrates two crucial features:

1. For any finite loss ($\eta < 1$), the scaling transitions from Heisenberg (\bar{n}^2) to standard quantum limit (\bar{n}) as \bar{n} increases.

2. The degradation is *gradual*—there is no catastrophic threshold as with NOON states.

The susceptibility for squeezed states scales linearly with \bar{n} :

$$\chi_F^{(\text{SQ})} \propto \bar{n}. \quad (\text{D6})$$

This linear scaling, combined with the SQL scaling of F_{SQ} , means the *relative fragility* χ_F/F remains constant, unlike for NOON states where it grows with N . This mathematical property underpins their reputation as the *tankers* of quantum metrology—robust, predictable, and optimal for steady-state sensing in lossy environments.

3. Temperature Sensitivity Considerations

For temperature estimation, the hierarchy manifests differently. Cat states encode temperature information in the *parity* of the interference pattern, which is more sensitive to dephasing than the phase information utilized by squeezed states. Consequently:

- **NOON states:** Maximally sensitive to both x and β but fragile to all noise channels.
- **Cat states:** Robust to amplitude damping but remain vulnerable to phase damping for temperature estimation.
- **Squeezed states:** Most robust to both damping channels for phase estimation, but suboptimal for temperature unless measured with non-Gaussian measurements.

4. Summary of the Metrological Hierarchy

Table II synthesizes these analytical results, providing a quantitative comparison of the three probe classes. The *Robustness Index* $\mathcal{R} = F_{\text{lossy}}/F_{\text{ideal}}$ at fixed $\epsilon = 0.1$ illustrates the practical performance degradation.

This hierarchy explains the experimental trade-offs observed in Sec. VI: while NOON states achieve the highest peak sensitivity, their fragility renders them impractical

for most real-world sensing applications. Cat states offer a compromise suitable for transient, non-Markovian environments, while squeezed vacuum states provide the optimal balance for steady-state sensing under realistic damping conditions.

ACKNOWLEDGMENTS

We acknowledge financial support from the Brazilian agencies: Coordenação de Aperfeiçoamento de Pessoal de Nível Superior (CAPES), financial code 001. NGA thanks FAPESP Grant 2024/21707-0.

[1] V. Giovannetti, S. Lloyd, and L. Maccone, Quantum-enhanced measurements: beating the standard quantum limit, *Science* **306**, 1330 (2004).

[2] V. Giovannetti, S. Lloyd, and L. Maccone, Quantum metrology, *Phys. Rev. Lett.* **96**, 010401 (2006).

[3] V. Giovannetti, S. Lloyd, and L. Maccone, Advances in quantum metrology, *Nature photonics* **5**, 222 (2011).

[4] M. G. Paris, Quantum estimation for quantum technology, *International Journal of Quantum Information* **7**, 125 (2009).

[5] G.-Y. Xiang and G.-C. Guo, Quantum metrology, *Chinese Physics B* **22**, 110601 (2013).

[6] G. Tóth and I. Apellaniz, Quantum metrology from a quantum information science perspective, *Journal of Physics A: Mathematical and Theoretical* **47**, 424006 (2014).

[7] C. L. Degen, F. Reinhard, and P. Cappellaro, Quantum sensing, *Rev. Mod. Phys.* **89**, 035002 (2017).

[8] V. Montenegro, C. Mukhopadhyay, R. Yousefjani, S. Sarkar, U. Mishra, M. G. Paris, and A. Bayat, Quantum metrology and sensing with many-body systems, *Physics Reports* **1134**, 1 (2025).

[9] H. Cramér, *Mathematical methods of statistics*, Vol. 26 (Princeton university press, 1999).

[10] L. M. Le Cam, *Asymptotic methods in statistical decision theory*, Springer series in statistics (Springer-Verlag, New York, 1986).

[11] H. L. van Trees, *Detection, Estimation and Modulation Theory, Part 1* (Wiley & Sons, 1968).

[12] C. W. Helstrom, Minimum mean-squared error of estimates in quantum statistics, *Physics letters A* **25**, 101 (1967).

[13] C. W. Helstrom, Quantum detection and estimation theory, *J. Stat. Phys.* **1**, 231 (1969).

[14] S. L. Braunstein and C. M. Caves, Statistical distance and the geometry of quantum states, *Phys. Rev. Lett.* **72**, 3439 (1994).

[15] J. S. Sidhu and P. Kok, Geometric perspective on quantum parameter estimation, *AVS Quantum Science* **2** (2020).

[16] C. Helstrom and R. Kennedy, Noncommuting observables in quantum detection and estimation theory, *IEEE Transactions on Information Theory* **20**, 16 (1974).

[17] P. A. Knott, T. J. Proctor, A. J. Hayes, J. F. Ralph, P. Kok, and J. A. Dunningham, Local versus global strategies in multiparameter estimation, *Physical Review A* **94**, 062312 (2016).

[18] E. Roccia, I. Gianani, L. Mancino, M. Sbroscia, F. Somma, M. G. Genoni, and M. Barbieri, Entangling measurements for multiparameter estimation with two qubits, *Quantum Science and Technology* **3**, 01LT01 (2017).

[19] J. Liu, H. Yuan, X.-M. Lu, and X. Wang, Quantum fisher information matrix and multiparameter estimation, *Journal of Physics A: Mathematical and Theoretical* **53**, 023001 (2020).

[20] G. Mihailescu, A. Bayat, S. Campbell, and A. K. Mitchell, Multiparameter critical quantum metrology with impurity probes, *Quantum Science and Technology* **9**, 035033 (2024).

[21] B. Xia, J. Huang, H. Li, H. Wang, and G. Zeng, Toward incompatible quantum limits on multiparameter estimation, *Nature Communications* **14**, 1021 (2023).

[22] Y. Yang, V. Montenegro, and A. Bayat, Overcoming quantum metrology singularity through sequential measurements, *Physical Review Letters* **135**, 010401 (2025).

[23] J. P. Dowling and K. P. Seshadreesan, Quantum optical technologies for metrology, sensing, and imaging, *Journal of Lightwave Technology* **33**, 2359 (2015).

[24] A. G. White, J. R. Mitchell, O. Nairz, and P. G. Kwiat, “interaction-free” imaging, *Physical Review A* **58**, 605 (1998).

[25] F. Yan, A. M. Iliyasu, and S. E. Venegas-Andraca, A survey of quantum image representations, *Quantum Information Processing* **15**, 1 (2016).

[26] S. Ahmadi, E. Saglamyurek, S. Barzanjeh, and V. Salari, High-contrast interaction-free quantum imaging method, *Physical Review A* **107**, 032611 (2023).

[27] J. R. Hance and J. Rarity, Counterfactual ghost imaging, *npj Quantum Information* **7**, 88 (2021).

[28] Z. Wang, M. Xu, and Y. Zhang, Review of quantum image processing, *Archives of Computational Methods in Engineering* **29**, 737 (2022).

[29] Y. Yang, V. Montenegro, and A. Bayat, Extractable information capacity in sequential measurements metrology, *Phys. Rev. Res.* **5**, 043273 (2023).

[30] H. Yang, Q. Zheng, P. Yue, and Q. Zhi, Quantum thermometry based on interferometric power, *Europhysics Letters* **146**, 38002 (2024).

[31] Z. Ou, Fundamental quantum limit in precision phase measurement, *Physical Review A* **55**, 2598 (1997).

[32] D. Yadav, G. Shukla, P. Sharma, and D. K. Mishra, Quantum-enhanced super-sensitivity of mach-zehnder interferometer using squeezed kerr state, *APL Quantum* **1** (2024).

[33] J. Grond, U. Hohenester, J. Schmiedmayer, and A. Smerzi, Mach-zehnder interferometry with interacting trapped bose-einstein condensates, *Physical Review A—Atomic, Molecular, and Optical Physics* **84**, 023619 (2011).

[34] M. Mehboudi, A. Sanpera, and L. A. Correa, Thermometry in the quantum regime: recent theoretical progress, *J. Phys. A* **52**, 303001 (2019).

[35] A. De Pasquale and T. M. Stace, Quantum thermometry, in *Thermodynamics in the Quantum Regime*, Fundamental Theories of Physics Ser. No. v.195, edited by

L. A. Correa, C. Gogolin, J. Anders, and G. Adesso (Springer International Publishing, 2018) p. 503–527, description based on publisher supplied metadata and other sources.

[36] L. A. Correa, M. Mehboudi, G. Adesso, and A. Sanpera, Individual quantum probes for optimal thermometry, *Phys. Rev. Lett.* **114**, 220405 (2015).

[37] S. Campbell, M. Mehboudi, G. D. Chiara, and M. Paternostro, Global and local thermometry schemes in coupled quantum systems, *New Journal of Physics* **19**, 103003 (2017).

[38] J. Rubio, J. Anders, and L. A. Correa, Global quantum thermometry, *Physical Review Letters* **127**, 190402 (2021).

[39] W.-K. Mok, K. Bharti, L.-C. Kwek, and A. Bayat, Optimal probes for global quantum thermometry, *Communications physics* **4**, 62 (2021).

[40] J. Glatthard, J. Rubio, R. Sawant, T. Hewitt, G. Bartolini, and L. A. Correa, Optimal cold atom thermometry using adaptive bayesian strategies, *PRX Quantum* **3**, 040330 (2022).

[41] M. Mehboudi, M. R. Jørgensen, S. Seah, J. B. Brask, J. Kołodyński, and M. Perarnau-Llobet, Fundamental limits in bayesian thermometry and attainability via adaptive strategies, *Phys. Rev. Lett.* **128**, 130502 (2022).

[42] G. Mihailescu, S. Campbell, and A. K. Mitchell, Thermometry of strongly correlated fermionic quantum systems using impurity probes, *Physical Review A* **107**, 042614 (2023).

[43] P. Sekatski and M. Perarnau-Llobet, Optimal nonequilibrium thermometry in markovian environments, *Quantum* **6**, 869 (2022).

[44] G. Planella, M. F. B. Cenni, A. Acín, and M. Mehboudi, Bath-induced correlations enhance thermometry precision at low temperatures, *Phys. Rev. Lett.* **128**, 040502 (2022).

[45] M. Płodzień, R. Demkowicz-Dobrzański, and T. Sowiński, Few-fermion thermometry, *Phys. Rev. A* **97**, 063619 (2018).

[46] E. Aybar, A. Niezgoda, S. S. Mirkhalaf, M. W. Mitchell, D. Benedicto Orenes, and E. Witkowska, Critical quantum thermometry and its feasibility in spin systems, *Quantum* **6**, 808 (2022).

[47] K. V. Hovhannisyan, M. R. Jørgensen, G. T. Landi, Á. M. Alhambra, J. B. Brask, and M. Perarnau-Llobet, Optimal quantum thermometry with coarse-grained measurements, *Prx Quantum* **2**, 020322 (2021).

[48] M. R. Jørgensen, J. Kołodyński, M. Mehboudi, M. Perarnau-Llobet, and J. B. Brask, Bayesian quantum thermometry based on thermodynamic length, *Phys. Rev. A* **105**, 042601 (2022).

[49] A. Ullah, Ö. E. Müstecaplıoğlu, and M. G. Paris, Optimizing quantum sensing networks via genetic algorithms and deep learning, *Quantum Science and Technology* **11**, 015031 (2025).

[50] A. Ullah *et al.*, Optimal strategies for transient and equilibrium quantum thermometry using gaussian and non-gaussian probes, *Phys. Rev. A* **112**, 062601 (2025).

[51] L. Ostermann and K. Gietka, Temperature-enhanced critical quantum metrology, *Phys. Rev. A* **109**, L050601 (2024).

[52] C. D. S. Brites, P. P. Lima, N. J. O. Silva, A. Millán, V. S. Amaral, F. Palacio, and L. D. Carlos, Thermometry at the nanoscale, *Nanoscale* **4**, 4799 (2012).

[53] L. Đačanin Far and M. D. Dramićanin, Luminescence thermometry with nanoparticles: A review, *Nanomaterials* **13**, 2904 (2023).

[54] M. Quintanilla, M. Henriksen-Lacey, C. Renero-Lecuna, and L. M. Liz-Marzán, Challenges for optical nanothermometry in biological environments, *Chem. Soc. Rev.* **51**, 4223 (2022).

[55] M. Fujiwara and Y. Shikano, Diamond quantum thermometry: from foundations to applications, *Nanotechnology* **32**, 482002 (2021).

[56] G. Kucsko, P. C. Maurer, N. Y. Yao, M. Kubo, H. J. Noh, P. K. Lo, H. Park, and M. D. Lukin, Nanometre-scale thermometry in a living cell, *Nature* **500**, 54 (2013).

[57] M. Scigliuzzo, A. Bengtsson, J.-C. Besse, A. Wallraff, P. Delsing, and S. Gasparinetti, Primary thermometry of propagating microwaves in the quantum regime, *Physical Review X* **10**, 041054 (2020).

[58] V. Montenegro, M. G. Genoni, A. Bayat, and M. G. Paris, Mechanical oscillator thermometry in the nonlinear optomechanical regime, *Physical Review Research* **2**, 043338 (2020).

[59] D. Burgarth, V. Giovannetti, A. N. Kato, and K. Yuasa, Quantum estimation via sequential measurements, *New Journal of Physics* **17**, 113055 (2015).

[60] V. Montenegro, G. S. Jones, S. Bose, and A. Bayat, Sequential measurements for quantum-enhanced magnetometry in spin chain probes, *Physical Review Letters* **129**, 120503 (2022).

[61] Y. Yang, V. Montenegro, and A. Bayat, Sequential-measurement thermometry with quantum many-body probes, *Physical Review Applied* **22**, 024069 (2024).

[62] L. Pezzé, A. Smerzi, G. Khoury, J. Hodelin, and D. Bouwmeester, Phase detection at the quantum limit with multiphoton mach-zehnder interferometry, *Physical review letters* **99**, 223602 (2007).

[63] D. Gatto, P. Facchi, and V. Tamma, Heisenberg-limited estimation robust to photon losses in a mach-zehnder network with squeezed light, *Physical Review A* **105**, 012607 (2022).

[64] C. Kumar, Rishabh, and S. Arora, Enhanced phase estimation in parity-detection-based mach–zehnder interferometer using non-gaussian two-mode squeezed thermal input state, *Annalen der Physik* **535**, 2300117 (2023).

[65] M. Abdellaoui, N.-E. Abouelkhair, A. Slaoui, and R. A. Laamara, Quantum phase estimation and realistic detection schemes in mach-zehnder interferometer using su (2) coherent states, *Physics Letters A* **522**, 129786 (2024).

[66] M. Verma, C. Kumar, K. K. Mishra, and P. K. Panigrahi, Advantage of non-gaussian operations in phase estimation via mach–zehnder interferometer, *Advanced Quantum Technologies* **8**, 2400192 (2025).

[67] A. Rai, D. Triggiani, P. Facchi, and V. Tamma, Heisenberg-scaling precision in the estimation of two parameters in a mach-zehnder interferometer, *Physical Review A* **111**, 062408 (2025).

[68] J. Preskill, Quantum computing in the nisq era and beyond, *Quantum* **2**, 79 (2018).

[69] J. M. Martinis, Qubit metrology for building a fault-tolerant quantum computer, *npj Quantum Information* **1**, 1 (2015).

[70] Z. Ma, P. Gokhale, T.-X. Zheng, S. Zhou, X. Yu, L. Jiang, P. Maurer, and F. T. Chong, Adaptive circuit learning for quantum metrology, in *2021 IEEE International Conference on Quantum Computing and Engineering (QCE)* (IEEE, 2021) pp. 419–430.

[71] K. Bharti, A. Cervera-Lierta, T. H. Kyaw, T. Haug, S. Alperin-Lea, A. Anand, M. Degroote, H. Heimonen, J. S. Kottmann, T. Menke, W.-K. Mok, S. Sim, L.-C. Kwek, and A. Aspuru-Guzik, Noisy intermediate-scale quantum algorithms, *Reviews of Modern Physics* **94** (2022).

[72] M. H. Devoret and R. J. Schoelkopf, Superconducting circuits for quantum information: An outlook, *Science* **339**, 1169 (2013).

[73] A. Blais, A. L. Grimsmo, S. M. Girvin, and A. Wallraff, Circuit quantum electrodynamics, *Rev. Mod. Phys.* **93**, 025005 (2021).

[74] IBM Quantum Development Team, Qiskit 1.1.0 (2024), accessed: 2025-03-23.

[75] IBM Quantum Development Team, IBM Quantum Documentation (2024), accessed: 2025-03-23.

[76] J. L. Beckey, M. Cerezo, A. Sone, and P. J. Coles, Variational quantum algorithm for estimation of the quantum fisher information, *Phys. Rev. Research* **4**, 013083 (2022).

[77] R. Kaubruegger, A. Rotondo, J. M. Zeiher, F. J. Gomez-Ruiz, I. Bloch, J. I. Cirac, and P. Zoller, Variational spin-squeezing algorithms on programmable quantum sensors, *Phys. Rev. Lett.* **123**, 260505 (2019).

[78] J. Meyer, M. Gärttner, and C. Henkel, Fisher information approach to nonequilibrium phase transitions in spin systems, *Phys. Rev. A* **102**, 052610 (2020).

[79] D. Y. Akamatsu, L. F. R. de Moura, G. G. Damas, G. D. de Moraes Neto, V. Montenegro, and N. G. de Almeida, Fundamental limits and experimental implementation of dispersive quantum thermometry, *Quantum Science and Technology* **10**, 045062 (2025).

[80] T. M. Stace, Quantum limits of thermometry, *Physical Review A—Atomic, Molecular, and Optical Physics* **82**, 011611 (2010).

[81] S. Razavian, C. Benedetti, M. Bina, Y. Akbari-Kourbolagh, and M. G. A. Paris, Quantum thermometry by single-qubit dephasing, *The European Physical Journal Plus* **134**, 284 (2019).

[82] M. Brunelli, S. Olivares, M. Paternostro, and M. G. Paris, Qubit-assisted thermometry of a quantum harmonic oscillator, *Physical Review A—Atomic, Molecular, and Optical Physics* **86**, 012125 (2012).

[83] E. Martín-Martínez, A. Dragan, R. B. Mann, and I. Fuentes, Berry phase quantum thermometer, *New Journal of Physics* **15**, 053036 (2013).

[84] C. Sabin, A. White, L. Hackermuller, and I. Fuentes, Impurities as a quantum thermometer for a bose-einstein condensate, *Scientific reports* **4**, 6436 (2014).

[85] A. White, L. Hackermuller, and I. Fuentes, Impurities as a quantum thermometer for a bose-einstein condensate, *Scientific Reports* **4** (2014).

[86] S. Campbell, M. G. Genoni, and S. Deffner, Precision thermometry and the quantum speed limit, *Quantum Science and Technology* **3**, 025002 (2018).

[87] A. Holevo, in *Quantum Probability and Applications to the Quantum Theory of Irreversible Processes* (Springer, 1984) pp. 153–172.

[88] F. Albarelli, I. Gianani, M. G. Genoni, and M. Barbieri, Fisher-information susceptibility for multiparameter quantum estimation, *Phys. Rev. A* **110**, 032436 (2024).

[89] B. M. Terhal, Quantum error correction for quantum memories, *Rev. Mod. Phys.* **87**, 307 (2015).

[90] A. Chatterjee, J. Schwinger, and Y. Y. Gao, Enhanced qubit readout via reinforcement learning, *Phys. Rev. Appl.* **23**, 054057 (2025).

[91] S. Braun, J. P. Ronzheimer, M. Schreiber, S. S. Hodgman, T. Rom, I. Bloch, and U. Schneider, Negative absolute temperature for motional degrees of freedom, *Science* **339**, 52 (2013).

[92] D. Frenkel and P. B. Warren, Gibbs, boltzmann, and negative temperatures, *American Journal of Physics* **83**, 163 (2015).

[93] L. Cerino, A. Puglisi, and A. Vulpiani, A consistent description of fluctuations requires negative temperatures, *Journal of Statistical Mechanics: Theory and Experiment* **2015**, P12002 (2015).

[94] R. J. de Assis, T. M. de Mendonça, C. J. Villas-Boas, A. M. de Souza, R. S. Sarthour, I. S. Oliveira, and N. G. de Almeida, Efficiency of a quantum otto heat engine operating under a reservoir at effective negative temperatures, *Physical review letters* **122**, 240602 (2019).

[95] J. Nettersheim, S. Burgardt, Q. Bouton, D. Adam, E. Lutz, and A. Widera, Power of a quasispin quantum otto engine at negative effective spin temperature, *PRX Quantum* **3**, 040334 (2022).

[96] E. Ivanchenko, Quantum otto cycle efficiency on coupled qudits, *Physical Review E* **92**, 032124 (2015).

[97] J.-Y. Xi and H.-T. Quan, Quantum heat engine and negative boltzmann temperature, *Communications in Theoretical Physics* **68**, 347 (2017).

[98] F. Campaioli, J. H. Cole, and H. Hapuarachchi, Quantum master equations: Tips and tricks for quantum optics, quantum computing, and beyond, *PRX Quantum* **5**, 020202 (2024).

[99] I. Afek, O. Ambar, and Y. Silberberg, High-noon states by mixing quantum and classical light, *Science* **328**, 879 (2010).

[100] J. A. Nielsen, J. S. Neergaard-Nielsen, T. Gehring, and U. L. Andersen, Deterministic quantum phase estimation beyond n00n states, *Physical Review Letters* **130**, 123603 (2023).

[101] B. M. Escher, R. L. de Matos Filho, and L. Davidovich, General framework for estimating the ultimate precision limit in noisy quantum-enhanced metrology, *Nat. Phys.* **7**, 406 (2011).

[102] S. L. Braunstein and P. van Loock, Quantum information with continuous variables, *Rev. Mod. Phys.* **77**, 513 (2005).

[103] B. Xia, J. Huang, H. Li, H. Wang, and G. Zeng, Toward incompatible quantum limits on multiparameter estimation, *Nature Communications* **14**, 1021 (2023).

[104] K. Park, T. Krisnanda, Y. Gao, and R. Filip, Quantum phase estimation beyond the gaussian limit, *arXiv preprint arXiv:2508.13046* (2025).

[105] T. M. Mendonça, D. O. Soares-Pinto, and M. Paternostro, Information flow-enhanced precision in collisional quantum thermometry, *Phys. Rev. Research* **7**, 043203 (2025).

[106] R. Bruck *et al.*, Low-loss silicon nitride waveguides for nonlinear integrated photonics, *Opt. Express* **28**, 24661 (2020).

[107] J. Qin, Y.-H. Deng, H.-S. Zhong, L.-C. Peng, H. Su,

Y.-H. Luo, J.-M. Xu, D. Wu, S.-Q. Gong, H.-L. Liu, *et al.*, Unconditional and robust quantum metrological advantage beyond n00n states, *Physical Review Letters* **130**, 070801 (2023).

[108] C. Monroe *et al.*, Programmable quantum simulations with trapped ions, *Rev. Mod. Phys.* **93**, 025001 (2021).

[109] K. R. Brown, C. Ospelkaus, Y. Colombe, A. C. Wilson, D. Leibfried, and D. J. Wineland, Coupled quantized mechanical oscillators, *Nature* **471**, 196 (2011).

[110] P. He, J. Shu, B. Xu, and J. Xu, Symmetric dicke states as optimal probes for wave-like dark matter, arXiv preprint arXiv:2512.14821 (2025).

[111] Y. Quek, S. Fort, and H. K. Ng, Adaptive quantum state tomography with neural networks, *npj Quantum Information* **7**, 105 (2021).

[112] L. Viola, E. Knill, and S. Lloyd, Dynamical decoupling of open quantum systems, *Physical Review Letters* **82**, 2417 (1999).

[113] J. Bylander, S. Gustavsson, F. Yan, F. Yoshihara, K. Harrabi, G. Fitch, D. G. Cory, Y. Nakamura, J.-S. Tsai, and W. D. Oliver, Noise spectroscopy through dynamical decoupling with a superconducting flux qubit, *Nature Physics* **7**, 565 (2011).

[114] C. E. Granade, C. Ferrie, N. Wiebe, and D. G. Cory, Robust online hamiltonian learning, *New Journal of Physics* **14**, 103013 (2012).

[115] V. Cimini, M. Valeri, S. Piacentini, F. Ceccarelli, G. Corrielli, R. Osellame, N. Spagnolo, and F. Sciarrino, Variational quantum algorithm for experimental photonic multiparameter estimation, *npj Quantum Information* **10**, 26 (2024).

[116] R. Yousefjani, S. Al-Kuwari, and A. Bayat, Discrete time crystal for periodic-field sensing with quantum-enhanced precision, *Phys. Rev. Appl.* **24**, 054047 (2025).

[117] T. J. Proctor, P. A. Knott, and J. A. Dunningham, Multiparameter estimation in networked quantum sensors, *Physical review letters* **120**, 080501 (2018).

[118] W. Ge, K. Jacobs, Z. Eldredge, A. V. Gorshkov, and M. Foss-Feig, Distributed quantum metrology with linear networks and separable inputs, *Physical review letters* **121**, 043604 (2018).

[119] R. Demkowicz-Dobrzański, J. Kołodyński, and M. Guță, The elusive heisenberg limit in quantum-enhanced metrology, *Nature communications* **3**, 1063 (2012).